JGR Earth Surface

RESEARCH ARTICLE
10.1029/2023JF007478

Impacts of Rainstorm Intensity and Temporal Pattern on Caprock Cliff Persistence and Hillslope Morphology in Drylands

Yuval Shmilovitz[1], Gregory E. Tucker[2,3], Matthew W. Rossi[2], Efrat Morin[1], Moshe Armon[4], Joel Pederson[5], Benjamin Campforts[6], Itai Haviv[7], and Yehouda Enzel[1]

[1]The Hebrew University of Jerusalem, The Fredy & Nadine Herrmann Institute of Earth Sciences, Jerusalem, Israel, [2]Cooperative Institute for Research in Environmental Sciences (CIRES), University of Colorado, Boulder, CO, USA, [3]Department of Geological Sciences, University of Colorado Boulder, Boulder, CO, USA, [4]Department of Environmental Systems Science, ETH Zurich, Zurich, Switzerland, [5]Geosciences Department, Utah State University, Logan, UT, USA, [6]Department of Earth Sciences, Vrije Universiteit Amsterdam, Amsterdam, The Netherlands, [7]Department of Earth and Environmental Sciences, Ben-Gurion University of the Negev, Be'er Sheva, Israel

Key Points:

- We developed a numerical model with explicit hydrology to study the evolution of arid cliffs in response to rainstorms
- Cliff height increases with decreasing cliff-debris grain size and increasing intensity of severe rainstorms
- Alterations in intra-storm intensity patterns, without a change in total rainfall, trigger hillslope geomorphic changes

Supporting Information:

Supporting Information may be found in the online version of this article.

Correspondence to:

Y. Shmilovitz,
yuval.shmilovich@mail.huji.ac.il

Citation:

Shmilovitz, Y., Tucker, G. E., Rossi, M. W., Morin, E., Armon, M., Pederson, J., et al. (2024). Impacts of rainstorm intensity and temporal pattern on caprock cliff persistence and hillslope morphology in drylands. *Journal of Geophysical Research: Earth Surface*, *129*, e2023JF007478. https://doi.org/10.1029/2023JF007478

Received 3 OCT 2023
Accepted 24 JAN 2024

Author Contributions:

Conceptualization: Yuval Shmilovitz, Gregory E. Tucker, Matthew W. Rossi, Efrat Morin, Moshe Armon, Joel Pederson, Itai Haviv, Yehouda Enzel
Formal analysis: Yuval Shmilovitz
Funding acquisition: Efrat Morin, Yehouda Enzel
Investigation: Yuval Shmilovitz, Matthew W. Rossi, Efrat Morin, Moshe Armon, Joel Pederson, Itai Haviv, Yehouda Enzel

Abstract Hillslope topographic change in response to climate and climate change is a key aspect of landscape evolution. The impact of short-duration rainstorms on hillslope evolution in arid regions is persistently questioned but often not directly examined in landscape evolution studies, which are commonly based on mean climate proxies. This study focuses on hillslope surface processes responding to rainstorms in the driest regions of Earth. We present a numerical model for arid, rocky hillslopes with lithology of a softer rock layer capped by a cliff-forming resistant layer. By representing the combined action of bedrock and clast weathering, cliff-debris ravel, and runoff-driven erosion, the model can reproduce commonly observed cliff-profile morphology. Numerical experiments with a fixed base level were used to test hillslope response to cliff-debris grain size, rainstorm intensities, and alternation between rainstorm patterns. The persistence of vertical cliffs and the pattern of sediment sorting depend on rainstorm intensities and the size of cliff debris. Numerical experiments confirm that these two variables could have driven the landscape in the Negev Desert (Israel) toward an observed spatial contrast in topographic form over the past 10^5–10^6 years. For a given total storm rain depth, short-duration higher-intensity rainstorms are more erosive, resulting in greater cliff retreat distances relative to longer, low-intensity storms. Temporal alternation between rainstorm regimes produces hillslope profiles similar to those previously attributed to Quaternary oscillations in the mean climate. We suggest that arid hillslopes may undergo considerable geomorphic transitions solely by alternating intra-storm patterns regardless of rainfall amounts.

Plain Language Summary Cliffs and escarpments in deserts are often shaped by rare and brief, but very heavy, rainstorms. However, over geologic time, it is difficult to evaluate topographic changes caused by such short-duration storms. Here we present a new model that simulates how a cliff forms and changes over time, through cumulative weathering and erosion. We conduct experiments to explore how the topography changes over the course of many rainstorms. The model results indicate that hillslope erosion and form are sensitive to magnitude of short rain bursts and to the size of cliff-derived rock fragments. A comparison of the model simulations with observations confirms that these two factors could explain spatial differences in cliff's form in the Negev Desert (Israel). Short-duration and high-intensity storms are associated with the persistence of cliffs and greater lateral retreat relative to longer, low-intensity storms. We conclude that hillslopes in arid areas may undergo significant topographic changes due to changes in the intensity and duration of rainstorms, even when the total rainfall amount remains unaltered.

1. Introduction

1.1. Background

Hillslopes form most of Earth's land surface and therefore their response to hydroclimatic forcings is a key factor to better understand landscape evolution. In drylands, hillslopes are often situated along cliff bands (Bryan, 1940; Duszyński et al., 2019; Dutton, 1882; King, 1953) and their evolution deviates from that of soil-covered hillslopes, where sediments are transported primarily by diffusion-like processes in the absence of overland flow (Howard

Methodology: Yuval Shmilovitz, Gregory E. Tucker, Matthew W. Rossi, Efrat Morin, Moshe Armon, Benjamin Campforts, Itai Haviv, Yehouda Enzel
Project Administration: Efrat Morin, Yehouda Enzel
Resources: Gregory E. Tucker, Efrat Morin, Yehouda Enzel
Software: Yuval Shmilovitz, Gregory E. Tucker
Supervision: Efrat Morin, Itai Haviv, Yehouda Enzel
Validation: Yuval Shmilovitz, Gregory E. Tucker
Visualization: Yuval Shmilovitz, Gregory E. Tucker, Matthew W. Rossi, Efrat Morin, Joel Pederson, Itai Haviv, Yehouda Enzel
Writing – original draft: Yuval Shmilovitz
Writing – review & editing: Yuval Shmilovitz, Gregory E. Tucker, Matthew W. Rossi, Efrat Morin, Moshe Armon, Joel Pederson, Benjamin Campforts, Itai Haviv, Yehouda Enzel

& Kochel, 1988; Howard & Selby, 1994, 2009; Schmidt, 2009). Rainstorms in deserts are a primary driver for changes at or near the Earth's surface at short time scales (Li et al., 2022; Naylor et al., 2017) as well as over time-scales of landscape evolution (Bull, 1991; Bull & Schick, 1979; Enzel et al., 2012; Yair & Lavee, 1990). Capturing hydro-geomorphic dynamics during short-lived (minutes to few hours) rainstorms is challenging as rainstorm-associated processes are infrequent, small-scale, and discontinuous (Goodrich et al., 1995; Marra & Morin, 2018; Sharon, 1979). Landscape evolution models (LEMs) constitute essential tools for understanding the effects of external forces on topography (Chen et al., 2014; Coulthard et al., 2013; Tucker & Hancock, 2010; Valters, 2016; Willgoose, 2005). However, conventional LEMs are commonly based on long-term-averaged (≫daily) climate forcing and simplified hydrological and erosion laws, which leave long-term geomorphic imprints of intra-storm hydrological and erosional interactions poorly understood (Skinner et al., 2020; Temme et al., 2017).

In this study, we develop a LEM for dryland hillslope profiles that incorporates an explicit representation of storm-scale hydrology and erosion. We first test the model under a control case of cliff degradation in which analytical solutions exist. We then examine hillslope response to rainstorm magnitude and to patterns of cliff weathering represented by the grain size of cliff-derived debris. A site-specific data-driven numerical experiment was conducted to examine the degree to which differences in storm magnitude and sediment size can explain the observed topographic differences along a 40-km hyperarid escarpment in the central Negev Desert, Israel. Last, we investigate long-term hillslope evolution under varying storm regimes of different rain intensity levels. The experiments reported herein quantify hydrogeomorphic processes on dryland hillslopes under short-duration rainstorms and their resulting topographic changes. This contributes insights toward developing testable and quantitative form-processes relations.

1.2. Dominant Processes on Dryland Hillslopes

Dryland hillslopes that are underlain by layered rocks often consist of a steep (near-vertical) resistant layer (commonly termed a caprock) that overlies a moderately inclined slope in less resistant rocks (lower slope, Figure 1). A primary erosional mode of hillslope evolution in drylands is lateral cliff retreat (Bryan, 1940; Dutton, 1882) caused by physical and chemical weathering processes such as freeze-thaw cycles (French, 2017; Schumm & Chorley, 1966), salt weathering (Goudie, 1993), and differential thermal stresses (Lamp et al., 2017) that disintegrate rock fragments in a way that maintains steep slopes (Kirkby, 1988). The material that falls from the cliff can range from grains (granular disintegration) to an entire rock slab (Schumm & Chorley, 1964; Terzaghi, 1962) depending on the release mechanism, caprock resistance, and joint spacing and size (Brunsden & Prior, 1984; Kirkby, 1988). The particle size of the collapsed debris varies from meter-scale blocks (Glade et al., 2017; Howard & Selby, 1994) to sand grains (in collapses with high energy and fragile lithologies) (Schumm & Chorley, 1964). Particle size in turn affects surface processes such as infiltration, runoff generation, and runoff-driven sediment transport (Greenbaum et al., 2020; Poesen & Lavee, 1994; Yair & Klein, 1973). Runoff is generated on the slopes mostly during high-intensity rainstorms and when the infiltration rate is lower than the rainfall rate (infiltration-excess mechanism, e.g., Wilcox et al., 1997). Even though it is infrequent, transportation of up to gravel-size material by Horton overland flow is a dominant mechanism (Bracken & Kirkby, 2005; Michaelides et al., 2012; Schmidt, 2009, 100 mm). In cases where the debris is larger than the maximum size that is transportable by overland flow, the removal of debris requires its prior breakdown into smaller pieces (Howard & Selby, 2009; Koons, 1955). Gravitation-controlled, creep-like debris transport is triggered on rocky desert slopes by rain-splash and other disturbance processes that can directly move centimeter-scale clasts on steep slopes (Bracken & Kirkby, 2005; Kirkby, 1988).

The evolution of rocky hillslopes, sometimes with heterogeneous lithology, is also known as scarp retreat: a process that has been a central theme in geomorphology for the last century (King, 1953; Kirkby, 1988; Koons, 1955; Wood, 1942). Previous conceptual models suggested that scarp evolution is controlled by the ratio between the rate of debris production from the caprock and the rate of debris breakdown and transport downslope from the lower layer to the pediment or stream (Ahnert, 1960; Carson & Kirkby, 1972; Schmidt, 2009; Schumm & Chorley, 1966). If sediment production outpaces evacuation, the cliff will be buried by its own debris (Selby et al., 1982). On the other hand, if sediment can be weathered and removed faster than it is produced, the lower slope will not be mantled by debris and free cliffs will persist (Carson & Kirkby, 1972; Schumm & Chorley, 1966). Base-level lowering through tectonic mechanisms and climate-driven changes in local geomorphic processes were suggested to alter the sediment budget, pacing the evolution of hillslope

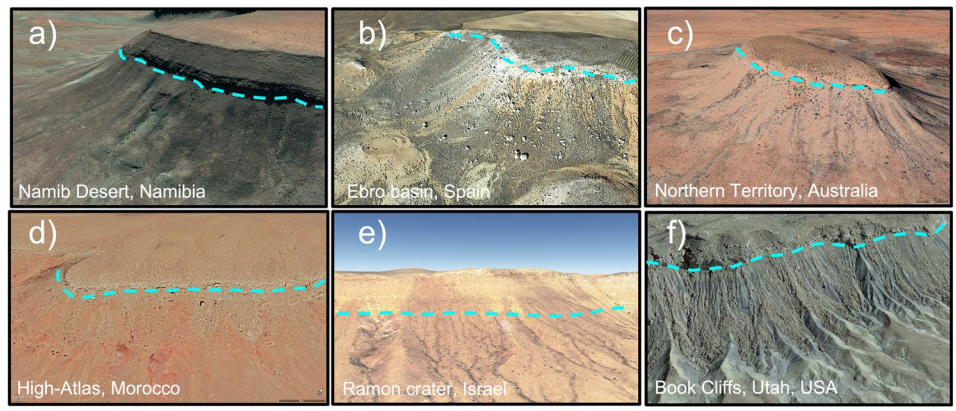

Figure 1. Examples of cliff-related hillslopes in various drylands. Cyan dashed lines approximate the lithological contacts between the caprock and the softer lower layers. (a) Basalt (caprock) over sandstone (lower layer), Namib Desert, Namibia (Lat: 25.5056, Lon: 16.8121, Airbus Landsat/Copernicus, 14 May 2014-newer). (b) Limestone over clay and marls, Ebro basin, Spain (41.3275, 2.2016 Landsat/Copernicus, 3 October 2018-newer). (c) Quartzite and meta-sedimentary rocks, Northern Territory, Australia (Lat: 22.7333, Lon: 130.5803, Maxar Technologies, Airbus, Landsat/Copernicus). (d) Limestone over claystone and marlstone, High Atlas, Morocco (Lat: 31.4918, Lon: 5.5746, Airbus, Landsat/Copernicus, 7 December 2022-newer). (e) Limestone and dolostone over sandstone, Ramon crater, Israel (Lat: 30.5143, Lon: 34.6501, Maxar Technologies, Mapa GISrael, Landsat/Copernicus, 22 February 2021-newer). (f). Sandstone over shale, Book Cliffs, Utah, USA (Lat: 38.9559, Lon: 109.8866, Landsat/Copernicus, 15 October 2022-newer). All images are from Google Earth.

landforms. Hillslope evolution without base-level lowering has piqued scientific curiosity for decades (Carson & Kirkby, 1972; King, 1953; Penck, 1953). However, with the exception of a few recent studies (Glade & Anderson, 2018; Glade et al., 2017; Ward et al., 2011), little attention has been paid to dryland rocky hillslopes and how climatic factors, and especially rainstorm properties, affect surface processes and topographic changes. There is a need to revisit these questions using tools from modern quantitative geomorphology; this gap stands at the center of this study.

1.3. Previous Associations Between Hillslope Evolution and Climatic Changes

The role of climate in hillslope evolution in drylands and associated surface processes has long been debated (Schmidt, 2009; Twidale, 1959; Twidale & Milnes, 1983). Although some researchers suggested viewing the evolution of dryland hillslopes in light of autogenic variations independent of climate variations (Bryan, 1940; Koons, 1955), others pointed out a strong link between hillslope evolution and climatic forcing at different scales, most commonly, at the scale of Quaternary glacial-interglacial cycles (Ahnert, 1960; Bull, 1991; Gerson, 1982). The relatively common, two-phase climatic-control model (Ahnert, 1960; Bull, 1991; Grossman & Gerson, 1987) suggests that during wet and cold climate phases, debris production increased by enhanced moisture availability, whereas debris evacuation was hindered by greater vegetation cover and gentler precipitation that hinder runoff generation and diffusion-like transport processes such as rain splash. Drier and hotter phases were hypothesized to be associated with decreasing sediment production and enhanced debris removal due to low vegetation cover and storms characterized by higher intensities, promoting slope dissection and cliff undermining. Dating of colluvial deposits in certain semi-arid regions has suggested that sediment accumulation tends to occur during the cold phases of Quaternary glacial cycles (Gutiérrez et al., 2006, 2010; Pena-Monné et al., 2022; Roqué et al., 2013; Sheehan & Ward, 2018). However, evidence from the arid Negev desert indicates that significant hillslope geomorphic transitions took place under continuous hyper-arid conditions and do not follow the proposed changes in the mean glacial-interglacial climates (Boroda et al., 2011). Rather, it was hypothesized that transitions between a stable phase in which the caprock and slope are debris-mantled, and a caprock-undermining phase (in which the debris-free sub-cliff slope is dissected), were driven by variations in frequency-magnitude relationships of erosion-effective high-intensity rainstorms (Boroda et al., 2013; Enzel et al., 2012), estimated by Shmilovitz et al. (2020) to reach or exceed the modern 100-year event. Changes in climate at scales that are finer than the general glacial-interglacial cycles were also recently suggested as the primary trigger for alternation between accumulation/evacuation phases in the Book Cliffs escarpment in the southwestern United States (McCarroll et al., 2021).

Progress toward understanding climatic influences on desert slopes requires a process-level perspective. However, to date, the quantification of rainstorm-scale rainfall effects on hillslope sediment budgets and associated long-term geomorphic imprints is still lacking. Here, we seek to fill this gap by focusing on the following research questions: (a) Under what conditions, in terms of rainstorm intensity and cliff-derived debris grain size, are cliffs preserved (or not)? (b) What are the effects of changes in the intra-storm temporal pattern of rain intensity on hillslope erosion, cliff persistence, and retreat? (c) Is there a recognizable relation between rainstorm regime and hillslope morphology? (d) How do alternating rainstorm regimes affect hillslope morphology? Answering these fundamental questions should lead to a better understanding of the controlling processes and their frequency of occurrences, and generate insights into how variability in rainstorm properties affects long-term hillslope evolution in drylands.

2. Approach

We model dryland hillslopes as landforms that evolve under the influence of short-duration (<24 hr) severe rainstorms (Shmilovitz et al., 2020). Accordingly, we developed a LEM that captures what we hypothesize to be the main hydrological and erosional processes activated by short-duration severe rainstorms. Incorporation of storm forcing and hillslope hydrology and geomorphology distinguishes our approach from previous hillslope LEMs (e.g., Anderson et al., 2019; Glade et al., 2017; Johnstone & Hilley, 2015) enabling us to investigate how rainstorm properties affect hillslope topography. The model distinguishes between two main lithological bedrock units: a resistant layer (caprock) that overlies a softer layer (lower layer). The model also includes a layer of mobile debris (debris layer, loosely consolidated granular material) with a thickness that can vary in space and time and may be zero (i.e., the bedrock surface is exposed at that point). As the grain size of cliff-derived debris plays a crucial role in surface processes in dry regions (Carson & Kirkby, 1972; de Figueiredo & Poesen, 1998; Howard & Selby, 2009), the debris layer in this study honors heterogeneous grain-size distributions sub-divided into various size classes.

During the simulations, the topography is updated according to four basic and commonly considered geomorphic processes: (a) production and ravel of debris from bedrock; (b) sediment transport by diffusion-like soil creep processes; (c) sediment transport by overland flow, and (d) incision of bedrock by overland flow. Given the disparity in time scales between landscape evolution (centuries to >millennia) and time scales of hydrological and overland flow processes such as runoff generation, infiltration, and sediment transport during storms (<minutes), it was necessary to compromise. As runoff-driven erosion in drylands is episodic, short-term, and associated with rare, high-intensity rainstorms, we run the model in an event-based framework. In such a framework, individual rainstorms are simulated, assuming that during inter-storm intervals, erosion by overland flow is negligible (cliff weathering and hillslope diffusion are considered during inter-storm intervals). By applying this approach, we were able to simulate a large number of rainstorms, for example, 1,000 rainstorms corresponding to rare storms characterized by a return period of 100 years (1% exceedance probability), and thus provide an estimation for the topographic change over 100 ka years. Figure 2 illustrates the model setup and the main processes it represents.

3. Model Description

3.1. Topographic Evolution

The model treats the temporal evolution of a topographic profile perpendicular to the strike of a hypothetical cliff. The model considers the evolution over time (t) of topographic elevation, $\eta(x, t)[L]$, at a given position along the profile, x, as the net balance of change in debris layer thickness, $H(x, t)[L]$, and bedrock elevation, $R(x, t)[L]$:

$$\frac{\partial \eta}{\partial t} = \frac{\partial R}{\partial t} + \frac{\partial H}{\partial t} \tag{1}$$

The thickness of the debris layer is updated according to the sum of the sediment flux by (a) overland flow transport, $q_s[L^2T^{-1}]$, (b) soil creep transport, $q_d[L^2T^{-1}]$, (c) underlying bedrock weathering, $W[LT^{-1}]$, and (d) local ravel and net flux of cliff-derived debris $D_{ls}[LT^{-1}]$:

$$\frac{\partial H}{\partial t} = \frac{1}{1-\phi_{sed}}(D_{ls} - W) - \nabla q_s - \nabla q_d \tag{2}$$

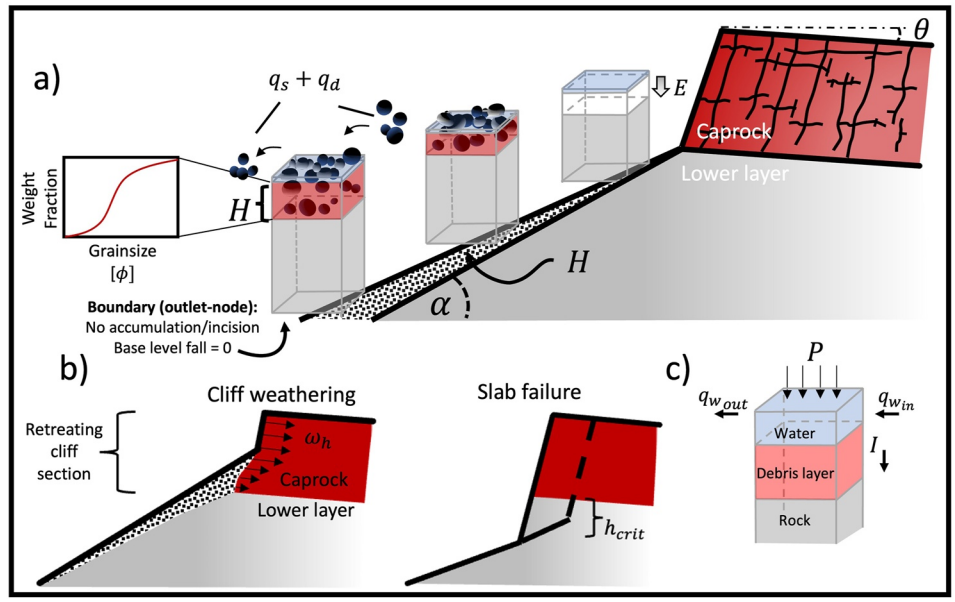

Figure 2. Model description. (a) General model setting separating the three major units represented by the model: an upper resistant layer (caprock), a lower softer layer, and a debris layer that varies in thickness (H) and comprises several grain size classes. Sediment transport includes size-dependent runoff-driven flux q_s and hillslope gravitational flux q_d. Erosion into the softer lower layer by overland flow, at rate E, occurs where there is no debris cover. The boundary condition at the outlet allows any runoff/sediment to be transported away (no accumulation) and the elevation at the base is held constant over time (no base level lowering/uplift). (b) A schematic of the presented cliff retreat mechanism. Cliff-normal weathering rate ω_h, is imposed on all cliff sections as a function of the debris cover. Downcutting into the softer layer results in slab failure of an entire rock slab based on the spacing of incipient fractures. (c) Hydrological processes represented by the model: P, is the 1-min resolution rainfall intensity, I is surface water infiltration, and q_w is the discharge flux from/to surrounding grid nodes.

where ϕ_{sed} is the sediment porosity. Bedrock elevation is a function of the weathering rate, W, and the bedrock erosion rate by overland flow $E[LT^{-1}]$:

$$\frac{\partial R}{\partial t} = E + W \tag{3}$$

3.2. Runoff-Driven and Hillslope Diffusion Transport

Sediment transport on drylands slopes occurs mainly by the combined action of wash processes and gravity. As the grain size of cliff debris ranges from sand to large boulders (Carson & Kirkby, 1972; Schumm & Chorley, 1966), commonly, only a portion of the sediment on the hillslope can be transported by overland flow (Howard & Selby, 2009; Michaelides et al., 2012). Therefore, we include a particle-size-dependent transport law in the runoff-driven transport equation. The runoff-driven sediment flux is calculated using the normalized volumetric sediment flux of the Meyer-Peter-Müller bed load transport equation (Meyer-Peter & Müller, 1948) that depends on the difference between the normalized bed shear stress and the critical Shields stress:

$$q^*_{s_i} = 8\left(\tau^*_i - \tau^*_{ci}\right)^{\frac{3}{2}} \frac{1}{1 - \phi_{sed}} \tag{4}$$

where $q^*_{s_i}$ is the volumetric dimensionless sediment flux of size class i, eight is the coefficient found by Meyer-Peter and Müller (1948), τ^*_i is the dimensionless normalized bed shear stress and τ^*_{ci} is the dimensionless critical Shields stress for sediment entrainment of size class i.

Field and experimental studies have shown that in a medium with grains of multiple sizes, the critical shear stress for the movement of a given particle depends not only on its absolute size but also on the surroundings

(Andrews, 1983; Ashworth & Ferguson, 1989; White & Day, 1982). To account for this effect, a mobility correction can be implemented in the form:

$$\tau_{c_i}^{*} = b\left(\frac{d_i}{d_{ref}}\right)^{\alpha} \tag{5}$$

where $\tau_{c_i}^{*}$ is the dimensionless critical stress for size fraction i, $d_i[L]$ is the particle diameter (commonly considered as the b-axis) and $d_{ref}[L]$ is a reference diameter (here selected as the median grain size in the grid node, $d_{ref} = d_{50}$), and b, α are empirical constants. Here we used $b = 0.086$ and $\alpha = -0.68$ following Komar (1987). The bed shear stress $\tau[Pa]$ is given by:

$$\tau = \rho g h_w S_w \tag{6}$$

where $\rho[ML^{-3}]$ is the fluid density, $g[LT^{-2}]$ is gravitational acceleration, $h_w[L]$ is the water depth, and $S_w[LL^{-1}]$ is the local water surface gradient. The normalized shear stress is defined as:

$$\tau_i^{*} = \frac{\tau}{(\rho_s - \rho) g d_i} \tag{7}$$

The dimensionless volumetric sediment flux can be converted to the actual volumetric flux by:

$$q_{s_i} = \begin{cases} q_{s_i}^{*}\left(\left(\frac{\rho_s - \rho}{\rho}\right) g d_i\right)^{0.5} d_i, & \tau_i^{*} > \tau_{c_i}^{*} \text{ and } H > 0. \\ 0, & \text{otherwise.} \end{cases} \tag{8}$$

where $\rho_s[ML^{-3}]$ is the sediment density. Dryland slopes can experience similar gravitational-controlled transport processes to those on soil-covered hillslopes, including rain splash (where vegetation is minimal), wet-dry cycles and freeze-thaw creep (where temperatures regularly cross the water freezing point). We compute the gradient-driven movement of sediments according to the local topographic slope with no dependency on the grain size:

$$q_d = \begin{cases} DS, & H > 0. \\ 0, & \text{otherwise.} \end{cases} \tag{9}$$

where $q_d[L^2T^{-1}]$ is the sediment flux by diffusion, $S[LL^{-1}]$, is the topographic slope, and $D[L^2T^{-1}]$ is transport efficiency (or diffusivity).

3.3. Bedrock Erosion

Bedrock incision is presumed to occur whenever the bedrock is exposed (defined where the thickness of the debris layer is zero). A common way to describe the erosion resistance of soft bedrock or soil is by a threshold shear stress, τ_{cb}[Pa], below which the rate of material detachment is negligible (Howard & Kerby, 1983):

$$E = \begin{cases} -k(\tau - \tau_{cb}), & \tau > \tau_{cb} \text{ and } H = 0. \\ 0, & \text{otherwise.} \end{cases} \tag{10}$$

where k is a bedrock erodibility coefficient, τ is the bed shear stress, and τ_c is the detachment critical shear stress.

3.4. Debris Production

In this model, cliff debris is produced by two processes: cliff weathering and caprock slab failure. We assume that mechanical weathering disintegrates caprock fragments in a way that maintains parallel retreat at a given horizontal rate $\omega_h[LT^{-1}]$. Then, the vertical descent rate $W[LT^{-1}]$ following the horizontal rate can be calculated:

$$W = \omega_h S. \tag{11}$$

To represent the protective role of sediment cover on the disintegration of bedrock fragments, we adopt one of the most commonly applied formulas for soil production, in which the sediment production rate from the underlying bedrock is an inverse-exponential function of soil thickness (Ahnert, 1976; Armstrong, 1976; Heimsath et al., 1997):

$$\omega_h = -W_h \exp^{-H/H_c} \tag{12}$$

where here $W_h[LT^{-1}]$ is the slope-perpendicular retreat rate for bare bedrock ($H = 0$) and $H_c[LT^{-1}]$ is a characteristic soil depth.

A failure of an entire caprock slab occurs when the layer beneath the caprock is exposed and the overlying caprock is undermined. We treat the undermining and collapse process as a discrete event that occurs when the topographic gradient between the caprock base and the adjacent downslope node exceeds a strength threshold (Glade et al., 2017; Ward et al., 2011). The thickness of the slab is defined by the incipient fracture spacing, assuming the fracture angle parallels the free cliff face at the beginning of the simulation (nearly vertical).

3.5. Transport and Deposition of Cliff-Derived Debris

Debris created by cliff weathering and/or slab failure is redistributed over the hillslope using a non-linear scheme proposed by Carretier et al. (2016), in which the sediment deposition rate declines as the slope increases toward an imposed threshold. This scheme is also non-local in the sense that sediment supplied from the upslope can continue downslope if the deposition rate is insufficient to deposit all the sediment:

$$D_{ls} = \frac{q_{ls}}{L} \tag{13}$$

where $D_{ls}[LT^{-1}]$ represents the deposition flux per area, and $q_{ls}[L^2T^{-1}]$ represents the landslide-derived sediment flux per unit width. The local transport distance $L[L]$ is calculated as:

$$L = \frac{\lambda}{1 - \left(\frac{S}{S_c}\right)^2} \tag{14}$$

where λ is a reference length scale for transport distance (here set to grid cell width Δx in the numerical solution), and $S_c[LL^{-1}]$ is a theoretically derived critical slope gradient. In our simulations, we assume S_c to be equal to the angle of repose of the debris material. When S approaches S_c, no deposition will occur at the considered grid cell. When $S > S_c$, L is considered effectively infinite, such that $D_{ls} = 0$ and there is no deposition at that grid cell.

3.6. Clast Fragmentation

We consider physical weathering as the dominant process for the in situ fragmentation of cliff-derived debris sediment. Assuming a negligible loss of material by chemical weathering, fragmentation can be described as a mass transfer from a parent particle to smaller daughter particles (Cohen et al., 2009, 2010). Physical fragmentation is implemented in the model following the mARM model approach (Cohen et al., 2009) in which the mass in each size-fraction is represented by a state vector, $G[W]$, and the change in grain size over time is derived by a transition matrix A:

$$G_{t+1} = G_t + \Delta F A G_t \tag{15}$$

The matrix A determines how many daughter fragments and to what sizes a parent clast splits into (the fragmentation pattern), and ΔF defines the fragmentation rate (how many parent clasts split) in each time step. Here we follow Cohen et al. (2009, 2015) in using a "split-by-half" fragmentation pattern (particles split into two equal-volume daughter fragments) for A, which shows a good fit to experimental and field data (Román-Sánchez et al., 2021; Wells et al., 2008).

3.7. Hydrology

Storms are represented in the model by time-varying, 1-min rainfall intensity, each lasting ~15–95 min. During each rainstorm, the model tracks the water volume in each grid-cell accounting for rainfall, infiltration, and overland flow routing. The water depth h_w is given by:

$$\frac{\partial h_w}{\partial t} = -\nabla q_{water} + P - I \tag{16}$$

where $q_{water}[L^2T^{-1}]$ is the water discharge per unit width, $P[LT^{-1}]$ is the rainfall intensity, and $I[LT^{-1}]$ is the infiltration rate of surface water into the soil. The water routing is modeled using a simplified form of the shallow-water equations that uses a numerical approximation to represent the momentum term (Adams et al., 2017; de Almeida et al., 2012). Infiltration is calculated following the Green and Ampt (1911) formula:

$$I = K_s \left[1 + \frac{(h_w + \psi_f)(\phi_{sed} - \theta_i)}{F}\right] \tag{17}$$

where $K_s[LT^{-1}]$ is the saturated hydraulic conductivity, $\psi_f[L]$ is the capillary pressure head at the wetting front, $F[L]$ is the cumulative infiltrated depth and θ_i is the initial soil moisture volumetric content.

4. Model Experiments

4.1. Numerical Implementation

The governing equations were solved on a 80–200 × 3 square raster grid (i.e., effectively, 1-D model, because the perimeter grid nodes are all treated as boundaries). The model is implemented in Python and built upon the existing Earth surface modeling platform Landlab (Barnhart et al., 2020; Hobley et al., 2017). Water infiltration and overland flow routing are calculated by the Landlab components SoilInfiltrationGreenAmpt (Rengers et al., 2016) and OverlandFlow (Adams et al., 2017), respectively. Dry-ravel of cliff-derived debris is calculated according to the sediment run-out component of the HyLands model (Campforts et al., 2020). All other processes in the model are implemented using new algorithms that are developed based on the Landlab platform.

4.2. Initial and Boundary Conditions

We set all boundaries except the lower edge of the slope to be closed, that is, not allowing the escape of runoff or sediment. The outlet at the base of the slope is held at a fixed elevation over time (i.e., no base level change). Any water or sediment reaching the slope outlet is assumed to be transported away, preventing water ponding or sediment aggradation at the lower boundary. All other edges of the domain are treated as no-flux (runoff/sediment) boundaries.

All experiments start with a nearly vertical cliff section, a lower layer with a constant slope beneath the cliff, and a 0.5 m thick debris cover. The initial nearly vertical cliff resembles an erosional scarp and is similar to the initial condition used in other hillslope-scale landscape evolution studies (Carson & Kirkby, 1972; Penck, 1953). The median grain size of the initial debris cover beneath the cliff was set to 10 mm, similar to the median grain diameter measured on arid pediment/alluvial surfaces (D'Arcy et al., 2017; Greenbaum et al., 2020; Shmilovitz et al., 2020). The masses of all other size fractions were distributed around the median size assuming a normal distribution with a standard deviation of 8 mm and the total grain mass was set to fit the 0.5 m thick debris cover. The caprock is slightly tilted (inclination = 1°–3°) in the opposite direction to the surface gradient adjacent to the lower layer (i.e., the cliff top does not drain to the lower layer). For simplicity, we only calculated water and sediment flow on the cliff-facing side of the domain.

4.3. Base-Line Parameters and Storm Input

As described above, we run the model with an event-based approach, in which short-duration rainstorms are simulated in a series, one by one. We define a reference storm, termed hereafter the "base-storm" (Figure 3), which is a 30-min-long storm that corresponds to a 100-year return period in the central Negev (Shmilovitz et al., 2023). The storm consists of three 10-min intensity bins and the maximal intensity for 10, 20, and 30 min

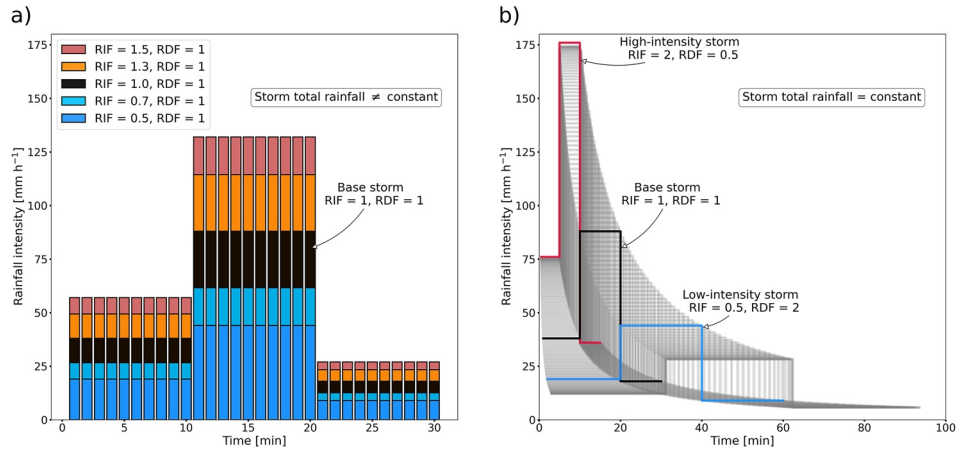

Figure 3. Hyetograph of the designed storms used in the model experiments. (a) Storms with varying total rainfall that were simulated in the experiment set (b) The black bins represent the 100-year storm in the central Negev (base-storm). (b) Storms that were simulated in experiments sets (c) and (d) (the total rainfall depth is the same for all storms). Red and blue solid lines show the high-intensity and low-intensity storms, respectively, given by the increase/decrease of magnitude (given by the rainfall intensity factor, RIF) and duration (given by the rainfall duration factor of the base-storm intensity bins (black solid line)). Gray solid lines are storms with various intensity levels that were simulated in experimental set (e).

represents the 100-year intensity (for those durations) as computed by an intensity-duration-frequency (IDF) curve (Figure S1 in Supporting Information S1). These bins were combined into a 30-min-long storm using the alternating block approach (Te Chow et al., 1988). We selected a duration of 30 min based on a typical duration for heavy rainfall events in the Negev (Shmilovitz et al., 2020). A duration of 30 min is also commonly used in physical rainfall experiments in drylands (Dunkerley, 2021). Our use of rainfall statistics from the Negev was not intended to "tune" our experiments to this region (except for experimental set c, see below), but rather to provide a reference and to ensure that simulated rainstorm properties are realistic. All of the other storms in our experiments were generated by scaling the base-storm intensity bins (see below). Between storms, we assume the soil is completely dry, as supported by the low frequency of rainfall events in drylands in contrast with the high rate of potential evaporation (Nicholson, 2011). Given the limited area of a single hillslope (commonly <0.5 km^2), we also assume that rain is uniformly distributed over the hillslope.

In each of the experiments, we set a constant rate for lateral cliff retreat, ω_h, of 10 mm between the simulated storms, which is similar to published rates in drylands considering storm return period of 50–100 years (Duszyński et al., 2019; Shmilovitz et al., 2022). In each simulation, we also determine the median size fraction of the cliff-derived debris (hereafter cliff-derived grain size, or CGS), assuming that the masses of all other size fractions are normally distributed around it using a coefficient of variation of 0.8 as found by field observations (Duller et al., 2010; Whittaker et al., 2010). In all of our simulations, CGS ranges between 0.01 and 1 m which is in agreement with clast measurements in the Negev (Shmilovitz et al., 2020, 2022) and other published values from the literature (Verdian et al., 2021). For tuning the fragmentation module to arid environments rate, we calibrate ΔF against surface clast measurements from dated arid alluvial surfaces (Figure S2 in Supporting Information S1). Infiltration parameters for the debris and lower layers were defined based on infiltration measurements and soil texture in the central Negev (Shmilovitz et al., 2023) and we assumed that no water infiltrates into the caprock. Table 1 summarizes the model parameters used in all simulations.

4.4. Experiments

We conduct five sets of model experiments. In each set, we conduct one or more experiments of 1,000–5,000 storms with different model configurations assumed as representing time intervals in the order of 100–500 thousand years.

4.4.1. Control-Run Experiment

The first experiment is a control run used to validate the modeled cliff retreat in comparison to the Fisher-Lehmann analytical model (Fisher, 1866; Lehmann, 1933). The Fisher-Lehmann model is one of the earliest analytical

Table 1
Experiments Parameter Table

Parameter	Description	Experiments set				
		Control	Sensitivity to rainfall intensity and grainsize	Data-driven	Single-storm type	Variable-storm type
Rows (–)	Domain rows	80	200	300	200	200
Columns (–)	Domain columns	3	3	3	3	3
dx (m)	Grid x spacing	1	1	1	1	1
dy (m)	Grid y spacing	1	1	1	1	1
nstorms (–)	Number of storms	–	1,000	1,500	5,000	4,000
H_c (m)	Debris production decay depth	–	0.5	0.5	0.5	0.5
ΔF (1/storm)	Debris fragmentation rate	–	10^{-4}	10^{-4}	10^{-4}	10^{-4}
K_s (m/s)	Debris layer infiltration rate	–	10^{-6}	10^{-6}	10^{-6}	10^{-6}
K_{sl} (m/s)	Lower layer infiltration rate	–	10^{-7}	10^{-7}	10^{-7}	10^{-7}
K_{sc} (m/s)	Caprock infiltration rate	–	10^{-10}	10^{-10}	10^{-10}	10^{-10}
ψ_f (m)	Capillary pressure head at the wetting front	–	0.28	0.28	0.28	0.28
ϕ_s (–)	Sediment porosity	–	0.2	0.2	0.2	0.2
ρ_s (kg/m^3)	Debris density	–	2,000	2,000	2,000	2,000
θ_i (–)	Initial soil moisture content	–	0.05	0.05	0.05	0.05
D (m^2/storm)	Hillslope diffusivity	–	0.03	0.03	0.03	0.03
n (–)	Manning's roughness	–	0.04	0.04	0.04	0.04
k_l (m^{2}s^2/kg)	Lower layer bedrock erodibility	–	$5 \cdot 10^{-5}$	$5 \cdot 10^{-5}$	$5 \cdot 10^{-5}$	$5 \cdot 10^{-5}$
k_c (m^{2}s^2/kg)	Caprock bedrock erodibility	–	10^{-10}	10^{-10}	10^{-10}	10^{-10}
τ_{cb} (Pa)	Lower layer bedrock critical shear stress	–	1	1	1	1
CH (m)	Initial caprock cliff height	50	15	100	15	15
θ (deg)	Caprock inclination	1	1	3	1	1
α (deg)	Lower layer slope	1	10	14	30	30
S_c (deg)	Critical slope gradient	40	33	33	33	33
W_h (m/storm)	Cliff weathering rate	–	0.01	0.02	0.01	0.01
CGS (mm)	Median grain size of cliff-derived debris	–	10, 50, 100, 1,000	60, 40	50	50
RIF (–)	Rainfall intensity factor	–	0.5, 0.7, 1, 1.3, 1.5	0.8, 1.2	0.5, 1, 2	0.31–2
RDF (–)	Rainfall duration factor	–	1	1	0.5, 1, 2	0.5–3.2

models for cliff degradation. It was later used and modified by others (Scheidegger, 2012), among them, the modification of Bakker and Le Heux (1947). There are a few fundamental assumptions that underlie these analytical solutions. First, no material is supplied to the slope from above its crest, and there is no removal of material from the toe. The retreat rate is assumed to be equal for all the exposed cliff bedrock, while beneath the accumulating debris, the bedrock is protected from further weathering. The resulting debris accumulates at the cliff foot as a rectilinear debris pile of constant angle. A few field experiments and observations support the validity of these analytical solutions (Bell & Fox, 1996; Hutchinson, 1998; Hutchinson & Stuart, 2003). We conduct a control-run experiment in which there is no hillslope transport either by overland flow or creep processes. As in the Fisher-Lehmann model, we defined bedrock weathering as zero where the debris layer is >0. We compare the simulated topography and bedrock profiles to the Fisher-Lehmann analytical solution (for an additional description see Text S1 in Supporting Information S1). For completeness, we also compare our result to the model of Bakker and Le Heux (1947).

4.4.2. Hillslope Morphology Sensitivity to Grain Size and Rainfall Intensity

We test how hillslope morphology changes in response to the grain size of sediment supplied from the cliff (the median grain size, CGS, is adjusted) and the rainfall intensity, which is adjusted by a rainfall intensity

factor (RIF). We focused on CGS and RIF because they are among the most widely discussed factors governing hillslope evolution in drylands (Ahnert, 1976; Carson & Kirkby, 1972; Howard & Selby, 2009). We conduct 20 model configurations of hillslope evolution under 1,000 rainstorms each, considering various combinations of CGS and RIF (the rainfall duration factor, RDF is held constant at 1). Changes in the CGS represent diverse scenarios in which the cliff breaks either into large fragments or small clasts, due to the potential influence of lithology, weathering process, and caprock fracturing pattern. The values of CGS (representing the median grain size) range between 10 and 1,000 mm and cover a wide range of published values of cliff-derived sediment grain size (Neely & DiBiase, 2020; Shmilovitz et al., 2022; Verdian et al., 2021). To examine the sensitivity to changes in the magnitude of rainstorms, we multiply the 10-min intensity bins of the base-storm by a RIF ranging between 0.5 and 1.5 (Figure 3a).

4.4.3. Data-Driven Experiments

We conduct data-driven numerical experiments based on rainstorm and grain-size data from the 40-km-long Ramon escarpment located in central Negev. The northern rim of the Ramon escarpment consists of hard carbonate rocks and is several to tens of meters high. The cliffs overlie erodible sandstone. There are no significant spatial lithological differences along the escarpment. The climate in the area is hyperarid (mean annual rainfall is 40–90 mm) along the escarpment and precipitation is characterized by discrete showers with extremely high inter-seasonal and annual variability. Between the southwest and northeast ends of Ramon escarpment northern rim (SWS and NES, respectively), there are pronounced differences in the morphology of the cliffs and slopes (Shmilovitz et al., 2023); the sub-cliff slopes at the SWS are longer and associated with milder gradients relative to shorter and dissected sub-cliff slopes of the NES with more debris-free sub-vertical bedrock patches. These differences were attributed to differences in the frequency of sediment mobilization driven by spatial variability in extreme rainstorm properties and grain size of cliff-derived sediment (Shmilovitz et al., 2023). The aim of this set of numerical experiments is to quantitatively investigate whether measured rainstorm properties and grain size of the cliff-derived debris could explain the observed topographic difference. In this experiments set, we conduct two simulations, each with RIF and CGS based on field measurements and local storm-scale rainfall statistics (Shmilovitz et al., 2023). All other parameters and initial conditions remained unchanged. For a description of how the initial conditions were determined based on the present topography see Text S2 in Supporting Information S1.

The fourth and fifth experiments sets aim to test the impact of rainstorm regimes and alternation between regimes on hillslope morphology. These sets were designed to represent changes in rainstorm regime that may have been induced by Quaternary-scale climatic changes, as proposed by earlier studies (Ben Dor et al., 2019; Boroda et al., 2011; Enzel et al., 2012).

4.4.4. Single-Storm Type Experiments

We designed three 5,000-storm-long model configurations of a single storm type. Each of these three configurations was conducted with a different rainfall intensity and duration factor, representing differences in the intra-storm intensity temporal distribution: (a) low-intensity storm regime (LI-storm regime), (b) base-storm regime (base-storm regime, identical to the above base-storm), and (c) high-intensity storm regime (HI-storm regime) (Figure 3). We consider changes in the intra-storm intensity distribution by changing the intensities of the base-storm 10-min intensity bins while still keeping the total storm rain depth constant. Constant storm depth was obtained by decreasing/increasing the duration of the intensity bins proportional to the increase/decrease in intensity. Keeping the total rainstorm depth constant assists in isolating the impact of intra-storm temporal intensity distribution on hydrogeomorphic processes. Obviously, determining the Quaternary-scale changes in storm structure is limited by available knowledge and by uncertainties characterizing past climates. Therefore, we implement changes in the storm structure based on general trends in maximal intensity during severe rainstorms and global warming. Studies have reported that short-duration (sub-hourly) maximal intensity during severe rainstorms increases with temperatures at rates higher than Clausius-Clapeyron scaling, and in the range of 10%–15% per degree Celsius (AghaKouchak et al., 2020; Attema et al., 2014; Fowler et al., 2021; Kendon et al., 2023; Lenderink & Van Meijgaard, 2008; Lenderink et al., 2021; Patricola et al., 2022; Westra et al., 2014). Considering Quaternary-scale temperature change of ±6° relative to today and 13% change per degree, we convert the base-storm to HI- and LI-storms by increasing and decreasing the intra-storm intensity bins (using the RIF), respectively, while maintaining the total storm depth constant by the corresponding decrease/increase in duration (using the RDF).

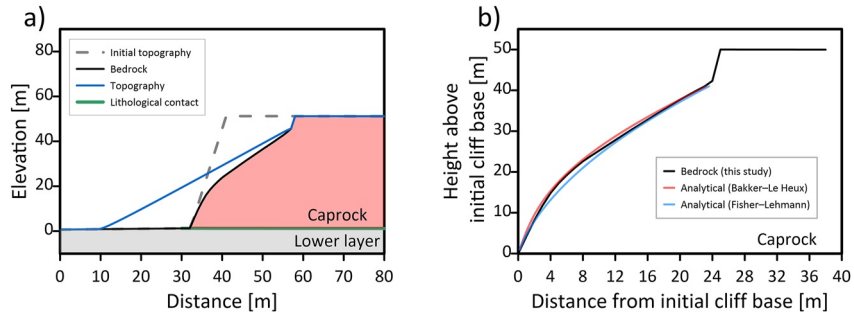

Figure 4. Cliff degradation under a no-transport case. (a) Modeled cross-sectional hillslope topography. The caprock and lower layer are represented by pink and gray shaded areas, respectively. The black solid line represents the bedrock surface and the blue line represents the topography at the end of the simulation. The dashed gray line represents the topography at the beginning of the simulation. (b) Model results compared with the predictions of the Fisher-Lehmann and Bakker-Le Heux cliff degradation models (only the caprock bedrock surface is presented). All models show a convex upwards bedrock profile beneath the debris cover.

4.4.5. Variable-Storm Type Experiments

We conduct three 4,000-storm-long experiments with alternation between hypothesized rainstorm regimes. In the first two experiments in this set, we vary between LI- and HI-storms (by varying the RIF and RDF over time). All storms hyetographs are shown in Figure 3 using a fixed sinusoidal perturbation with periods of 2,000, and 1,000 storms. In the third experiment, we use the Quaternary-scale temperature record of Jouzel et al. (2007) to scale a 4,000-storm record, assuming a 13% of increase/decrease per °C (as before). Similar to above, the rainstorms vary in the temporal intensity pattern but we fixed the total rainfall depth.

5. Results

5.1. Control-Run Experiment: Scarp Profile Without Transport on the Slope

Figure 4 presents the model result for cliff degradation under the assumptions of the Fisher-Lehmann model. It can be observed that, in the model, as the debris accumulates beneath the cliff, the bedrock-debris contact evolves into a convex-upward profile, with its upper parts tangent to the debris angle of repose. The modeled profile of the bedrock-debris contact is fairly similar to Fisher-Lehmann and Baker-Lahuex analytical solutions.

5.2. Sensitivity of Hillslope Morphology to Cliff-Derived Debris Size and Rainfall Intensity

Hillslope morphology based on multiple combinations of median grain size (CGS) and RIF are shown in Figure 5. When the base-storm intensities are reduced by a factor of 0.5 (i.e., RIF = 0.5, Figure 5a, left column), the cliff height (defined as the height of debris-free caprock) at the end of the simulation is <40% of the initial height (Figure 5b). This indicates that when rainfall intensities are low, even if the cliff weathering processes produce debris with small particles, the flux of sediment carried by the overland flow is smaller than the flux of sediment delivered from the cliff; thus, the cliff gets buried. The burial of the cliff is also observed when CGS is large (1-m median diameter), regardless of RIF (Figure 5a, right column). Under the scenarios of CGS <1,000 mm, the overall morphology and the cliff height at the end of the simulation are highly dependent on RIF. As RIF increases, the debris covers a smaller area of the cliff, and the slope concavity increases (Figure 5a). When the RIF is ≥1 and CGS = 10 mm (Figure 5a, lower-right corner), the softer layer is incised by the overland flow, the cliff is free of debris (the cliff height at the end of the simulation is 100%, Figure 5b), and undermining drives continued retreat. Under RIF ≥1, incision of the lower layer is observed at the lower parts of the slope even when the CGS is large (>100 mm, Figure 5a) because sediments are not transported down the slope and the lower layer surface remains unprotected by a debris cover.

The cliff-derived debris size and rainfall intensity have a pronounced impact on sediment transport dynamics and grain-size distribution along the hillslope (Figure 6). Simulations with low rainfall intensities (Figure 6, lower row) are associated with an abrupt change in particle size at a distance of ~60 m from the outlet, which is the bottom of the cliff-derived debris pile. The abrupt change in particle size is associated with a break-in-slope that

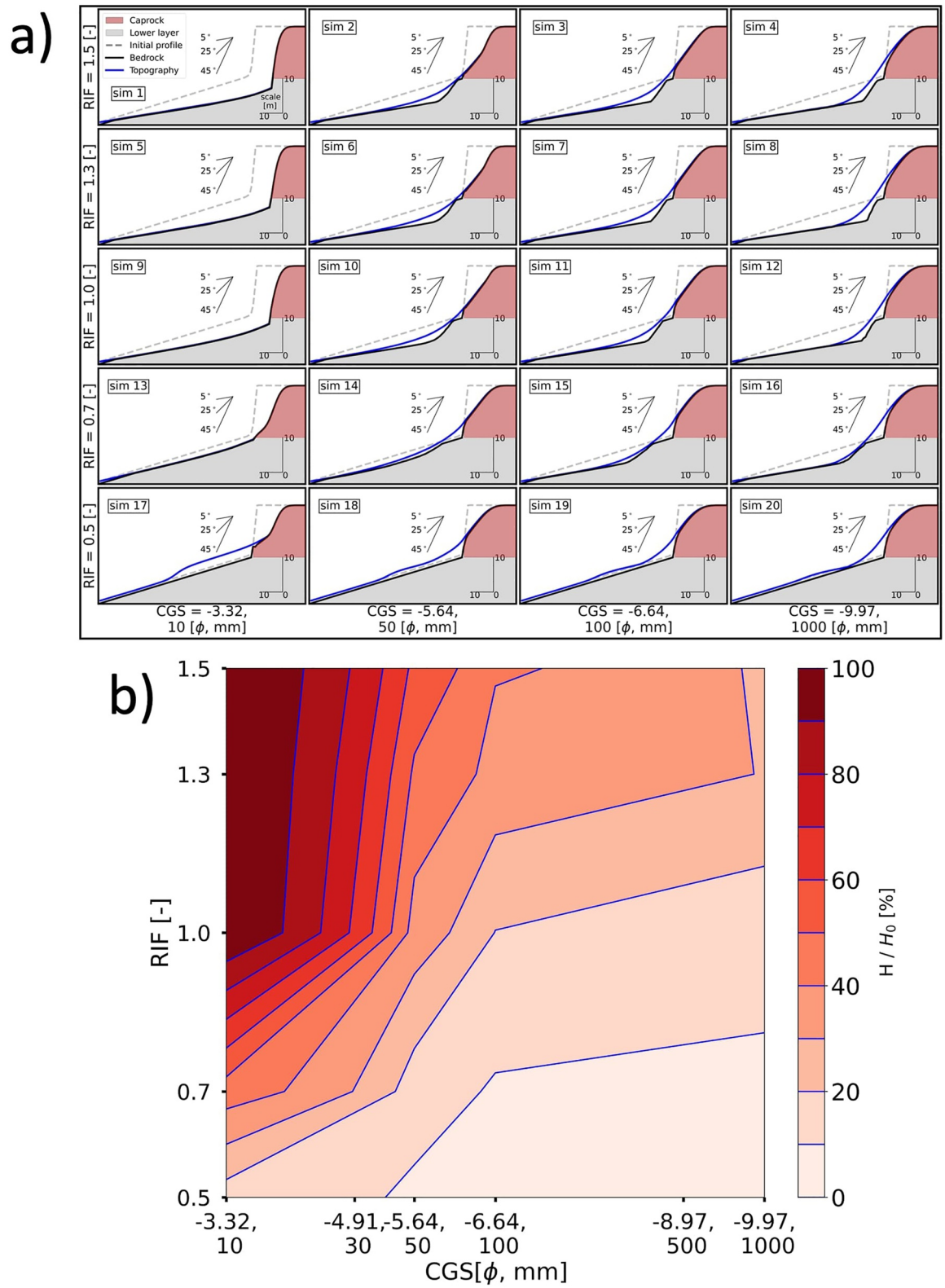

Figure 5. Hillslope simulated topography after 1,000 storms as a function of rainstorm intensity factor (RIF) and cliff-derived sediment grain size (CGS). (a) End-of-simulation hillslope profiles at varying values of RIF (columns) and CGS (rows). Symbols and colors are the same as in Figure 4. (b) Heat map of end-of-simulation caprock cliff height relative to the initial cliff height as a function of CGS (*y*-axis) and RIF (*x*-axis).

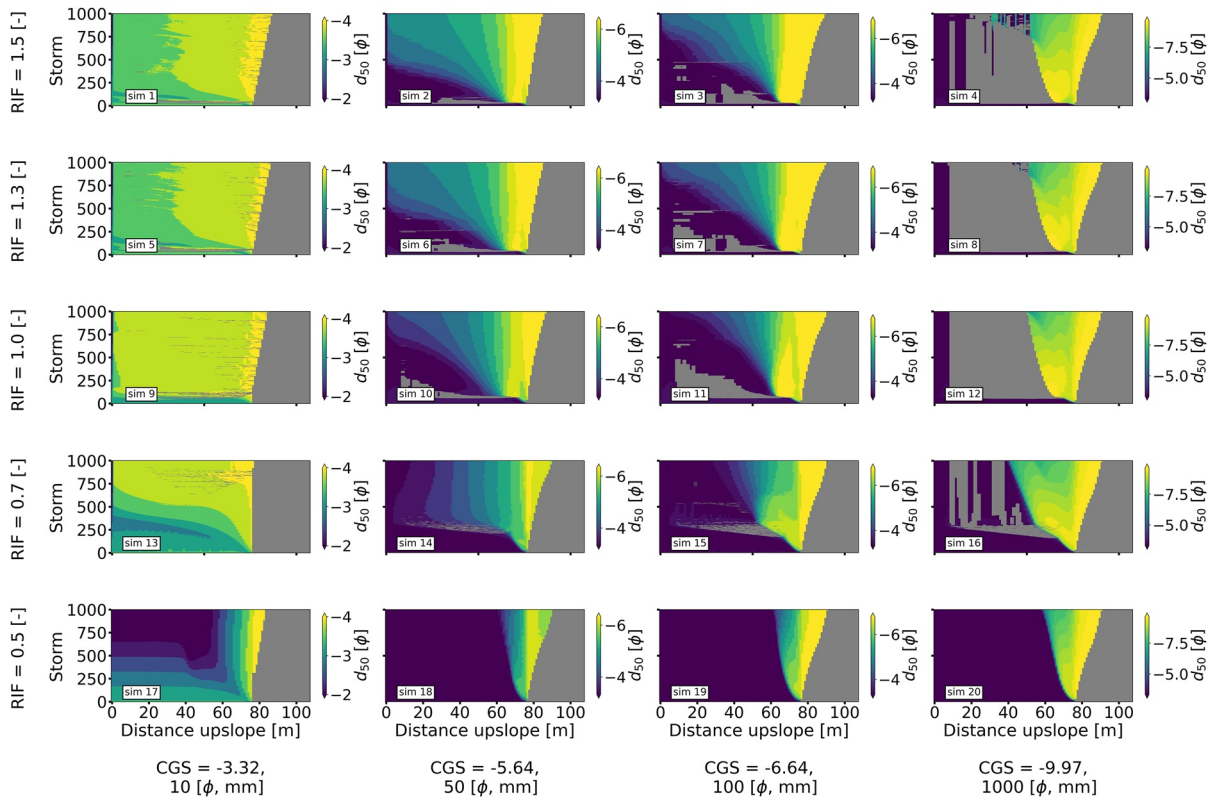

Figure 6. Space-time diagrams at varying values of rainstorm intensity factors (RIF, columns) and cliff-derived grain size (CGS, rows), presenting grain size (d_{50}) distribution along the hillslope (for the same experiments presented in Figure 5a). The *x*-axis in every figure is the distance upslope and the *y*-axis is the storm number. Colors denote the median grain size and gray areas are locations with no debris cover (color bars differ in scale).

separates the milder lower slope-pediment and, the upper coarser and steeper talus-slope. Decreasing CGS and/or increasing RIF smoothed this transition and under RIF >1 and CGS <50 mm, a smooth concave upward profile is observed. When the RIF≥1 (less pronounced for the simulation with CGS of 10 mm, Figure 6 left column), there is a general decrease in grain size down the slope. The resulting grain-size pattern reflects size-dependent transport and deposition along the slope. When CGS = 10 mm, sediment mobilization is relatively homogeneous along the slope (>10 mm, Figures 7a and 7d). Conversely, when the cliff supplies coarse debris (CGS >10 mm), small to medium-size grains are transported from the upper parts, leaving the larger sediment behind (>60 mm Figures 7b, 7c, 7e, and 7f). For example, at a distance of 75 m from the outlet (blue lines in Figures 7b and 7c), up to 60 mm grains are transported downslope (solid blue lines in Figures 7b, 7c, 7e, and 7f) and the d_{50} at the end of the simulation is relatively large (blue circle in Figures 7b and 7c). At the lower parts of the slope (yellowish lines in Figures 7b, 7c, 7e, and 7f), however, medium-size particles (>11–50 mm) are deposited (Figures 7b and 7c) and the d_{50} at the end of the simulation is much smaller (Figures 7b and 7c).

5.3. Data-Driven Experiments: Could Spatial Differences in Grain Size of Cliff Debris and Rainstorm Intensity Induce Topographic Differences Along the Ramon Escarpment?

As discussed above, the exposure of vertical cliff and debris cover on the hillslope is strongly affected by the cliff debris grain size and the rainfall intensity. In the data-driven experiments set, we test whether these two parameters (RIF and CGS) are capable of explaining the observed topographic differences along the 40-km Ramon escarpment (central Negev, Israel, Figure 8c). The model results broadly mirror the observed topographic differences between the two ends of the Ramon escarpment: a thicker and higher debris cover is developed at the southwestern side (SWS) of the Ramon escarpment relative to the thin debris cover and exposed vertical cliff on the northeast side (NES, Figures 8a and 8b). While the upper parts of the simulated NES slopes are similar to the measured profiles, below the caprock, the simulated profile deviates significantly from the measurements and is predicted to be much lower (Figure 8b). Note that in order to isolate the influence of rainfall intensity

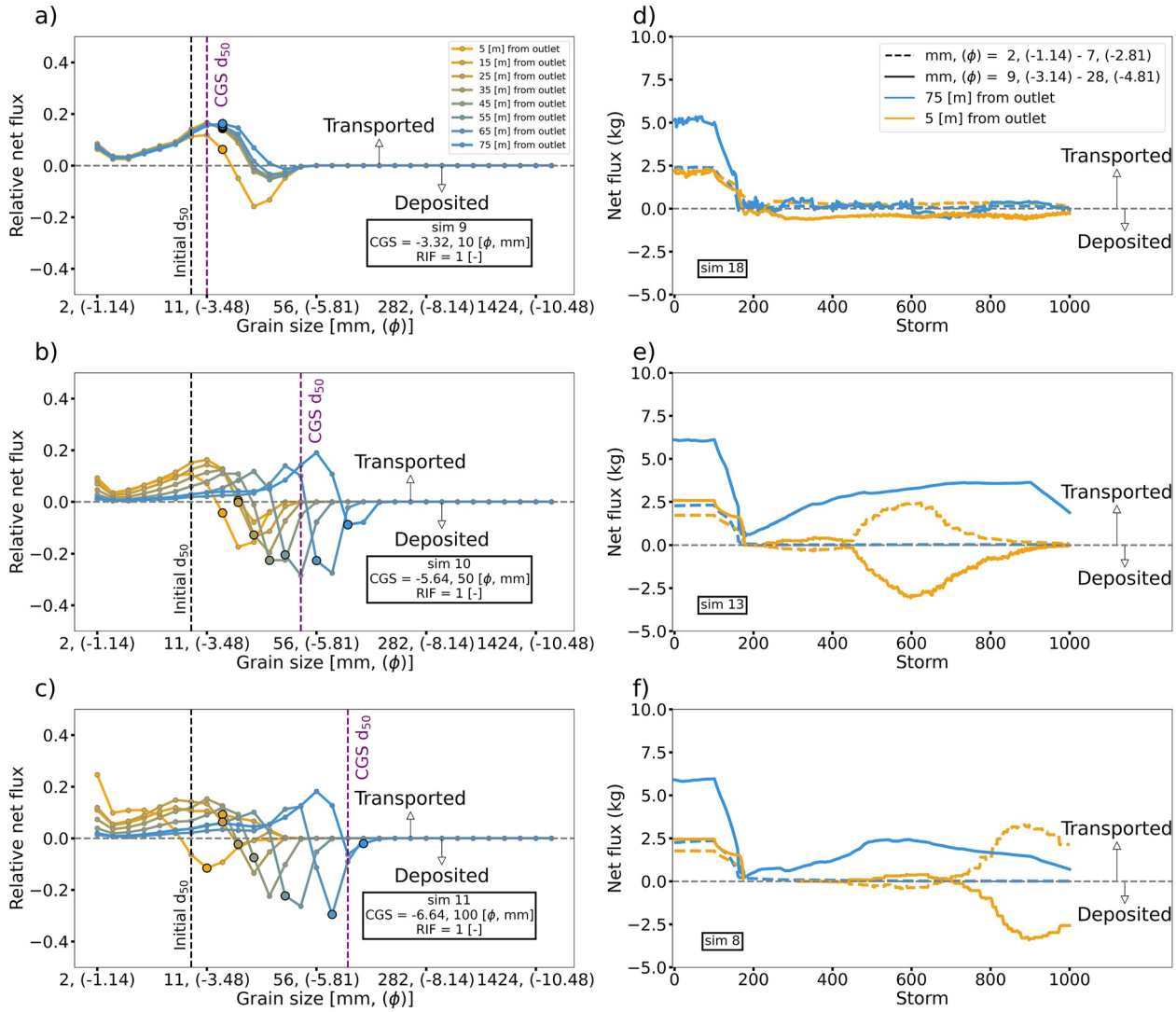

Figure 7. Examples of hillslope runoff-driven, size-dependent sediment transport. Panels (a–c) present size-dependent sediment flux for three model experiments with different cliff-derived grain size (CGS; 10, 50, and 1,000 mm, respectively). Colored lines are storm-accumulated net sediment flux as a function of grain size (the net flux for each size fraction divided by the total net flux; positive values indicate net transport and negative values indicate net deposition) at several distances from the outlet (colors). The colored circles show the d_{50} at the end of the simulation (x-axis only). Vertical dashed black and purple lines show the initial d_{50} and the CGS, respectively. The relatively homogeneous end-of-simulation grain size in panel (a) results from the homogeneous transportation of small grains (<11 mm) downslope and deposition of medium-sized grains under the case in which the cliff-debris grain size is small. In panels b and c, there is almost no deposition of material by overland flow in the uppermost part of the slope (>65 m from the outlet) while small-to-medium size grains are deposited downslope. Toward the outlet, the minimal deposited grain size is getting smaller. The end-of-simulation d_{50} decreases downslope due to the transportation of small-medium grains from the upper parts, their deposition at the lower parts, and the supply of large material by dry ravel in the upper parts. Panels (d–f) show the net sediment flux (in kg, for the same experiments as in panels (a–c), respectively) of 2–7 mm (dashed lines) and 9–28 mm (solid lines) grains at 5 and 75 m from the outlet (orange and blue lines, respectively). In panel d, deposition, and transport patterns are similar at both locations, indicating a relatively homogeneous transport. In panels (e) and (f), 9–28 mm grains are transported from the upper parts of the slope (solid blue line) and deposited downslope (solid orange line). The 2–7 mm grains are transported from both locations at the beginning of the simulation.

and debris grain size, the initial conditions in all of the simulations in this experiment are the same and were based on the SWS topography (Figure S6 and Text S1 in Supporting Information S1) since it is associated with thicker debris cover and less susceptible to undermining (the latter makes determining the initial conditions difficult). It is possible to better match the NES topography by applying different initial conditions (Figure S5 in Supporting Information S1) and potentially even more by calibrating parameters such as hydraulic conductivity and/or changing the conditions at the boundary. Also, here we did not consider differences in weathering and clast fragmentation rates although they probably vary between the sites as a function of the local temperatures (Gaillardet et al., 2019), especially when considering Quaternary-scale temperature variation (Shmilovitz

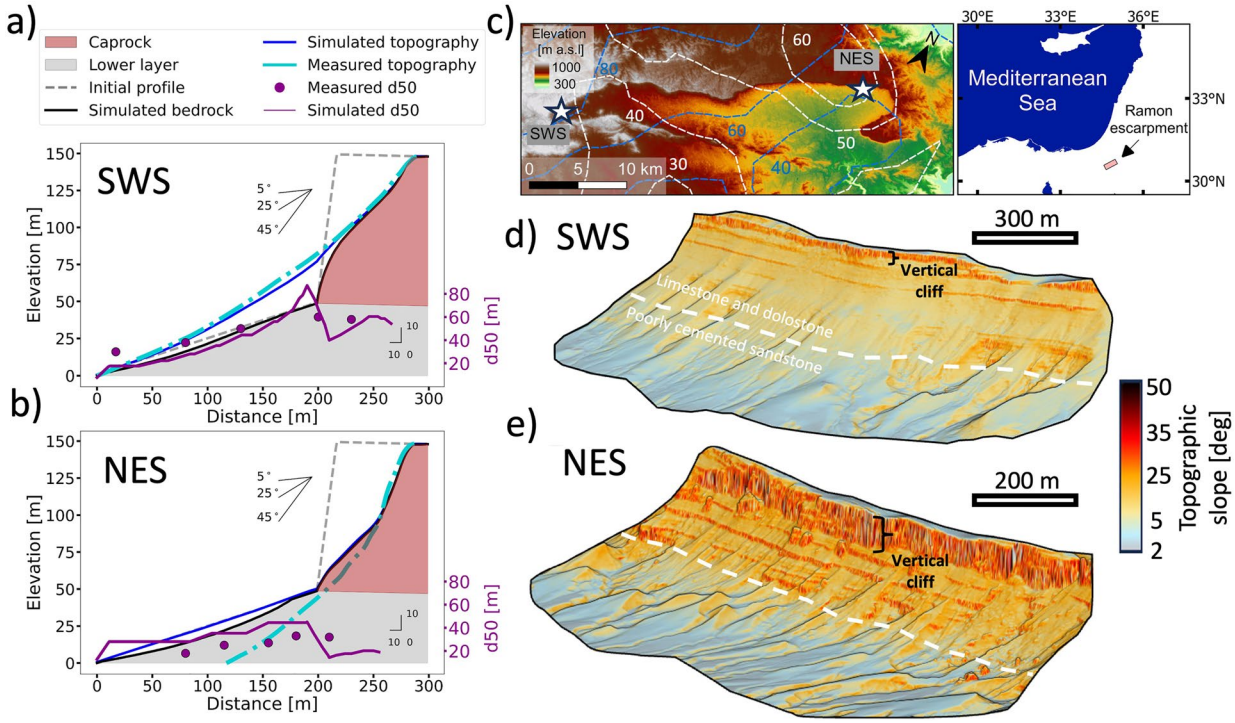

Figure 8. Field-driven experiment results. (a, b) Comparison of model results and measured topography and sediment grain size for the SWS and NES sites, respectively. Symbols and colors are as in Figure 4a. The cyan dashed line represents the measured topography, the purple solid line represents the modeled d_{50} and the solid purple dots show the measured d_{50} as derived from point counts (Shmilovitz et al., 2023). (c) Digital elevation model of Ramon escarpment. White stars denote the two study sites. Blue dashed lines are isohyets (in mm) representing annual rainfall (Shmilovitz et al., 2023). White dashed lines represent the 100-year rainfall intensity (in mm h^{-1}) for 30 min. The map on the right shows the location of Ramon Escarpment. (d, e) Digital elevation models and topographic slope for the SWS and NES sites in Ramon escarpment, respectively.

et al., 2023). Despite the aforementioned topographic mismatch, the general differences between the sites emerge, including the general decrease in grain size down the slope in both sites. Thus, the combination of only two parameters, CGS and RIF, appears to be sufficient to account for the observed topographic differences along the Ramon escarpment.

5.4. Single-Storm Type Experiments

The influence of intra-storm intensity patterns on hillslope morphology and retreat was first explored by three simulations of 5,000 storms of the same type, each with a different intensity level (Figure 9). Hillslope morphology, grain-size distributions, and cliff retreat vary significantly with respect to the storm intensity level. Under the LI-storm regime, the cliff becomes buried quickly after 1,000 storms, and its upper parts are covered by a thin veneer of debris (Figures 9a and 9d). With the increase in intensity level, more debris is evacuated and vertical cliffs persist longer. Under the base-storm regime, the burial of the cliff starts after 2,000 storms, as the slope length and its gradient decrease (Figures 9b and 9e). Under the HI-storm regime, the cliff is repeatedly undermined throughout the simulation and its retreat distance is the longest (Figures 9c and 9f). In both the base- and HI-storm regimes, the greater transport of sediment by the overland flow on the slope is also responsible for a more pronounced down-the-slope decrease in grain size. HI-regime exhibits greater transport due to higher maximal shear stresses exerted by overland flow over the entire slope, relative to the local high shear stress at the middle part of the slope in the Base- and LI-regimes (Figure S4 in Supporting Information S1).

5.5. Variable-Storm Experiments

In this section, we test the impact of long-term changes in storm regimes on hillslope morphology. First, we applied fixed sinusoidal oscillations between HI- and LI-storms, with each oscillation characterized by a period of 2,000 and 1,000 storms (Figure 10). When the cycle duration is 1,000 storms (Figures 10b and 10e), the

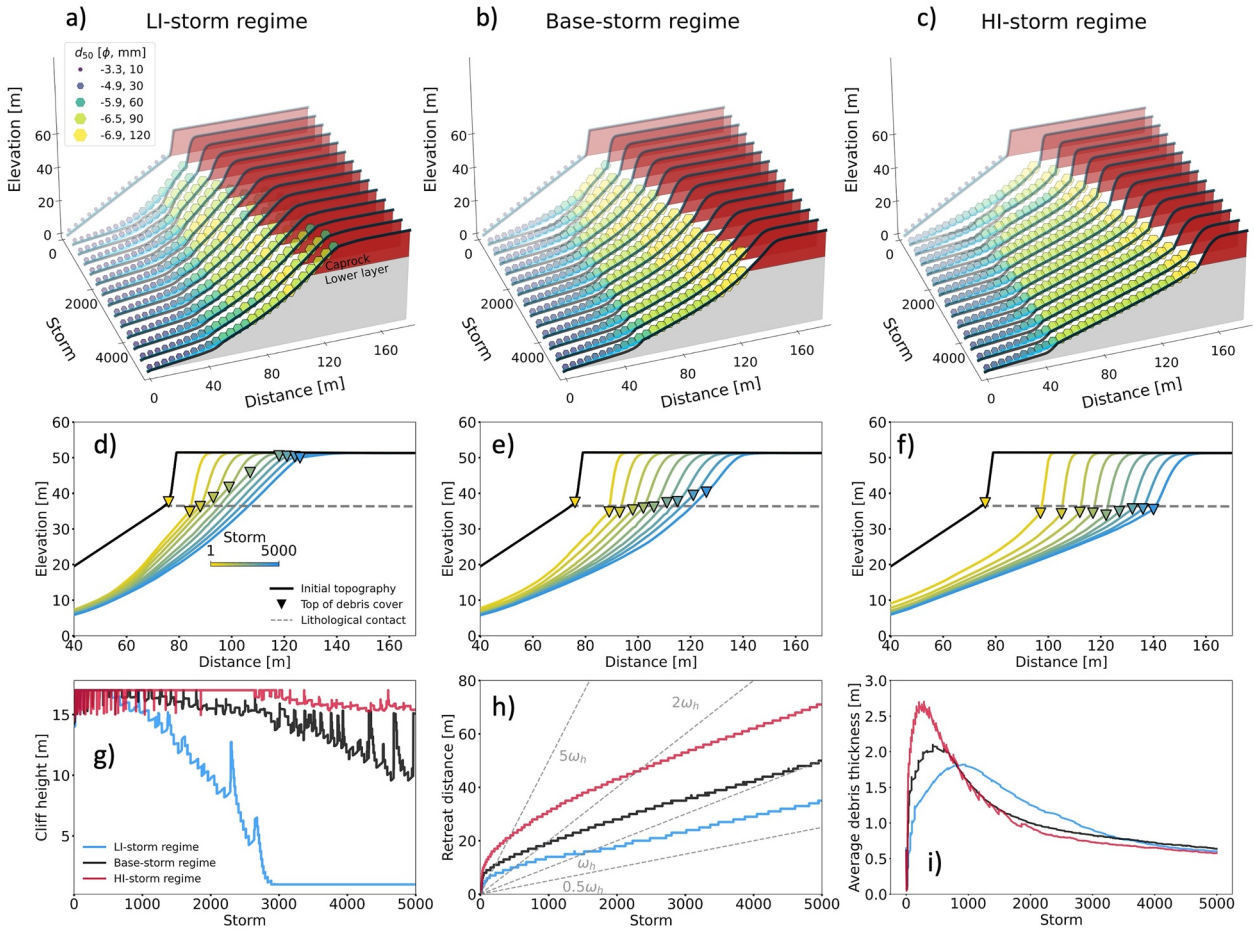

Figure 9. Changes in hillslope morphology and grain size during the three single storm experiments: (a) low-intensity storm regime, (b) base-storm regime, (c) high-intensity storm regime. Panels (d–f) show the hillslope topographic profiles and the uppermost extent of debris-cover (opposite triangles) along the slope of the respective experiment as in (a–c) respectively. Panels (g–i) show changes in exposed cliff height, retreat distance, and average debris thickness during each of the experiments. Gray lines in panel (h) show retreat distances for several constant weathering rates relative to the base rate (w_h) applied in all experiments.

debris is efficiently evacuated and the cliff is undermined and retreats for a longer distance. However, when the oscillation period interval is 2,000 storms, the thickness of the debris cover above the lithological contact varies throughout the simulation (Figures 10a and 10d). Accumulation of debris and partial covering of the cliff occur during intervals of LI- (RIF <1), whereas during HI-storms (RIF >1), debris is removed. During cycles characterized by partial cliff covering and exposure, there are times when a slope break in the caprock is generated in the simulated topographic profile (e.g., storm 2,200 in Figure 10a). A sharp break in the slope in the caprock marks the boundary between the upper part of the cliff that was not covered by debris and the lower part that was covered and later on, was exposed. In all the simulations, the grain-size distribution on the slope changes with the alternating storm regimes; a higher degree of downslope sorting is observed during intervals characterized by high-intensity storms.

Similar patterns regarding the extent of the debris cover and the grain-size distribution are observed in the experiment with variable storm intervals, scaled by the temperature record (Figures 10c, 10 f, and 10i). Breaks in the caprock slope are observed, for example, in storms 1,700 and 2,720. Since this experiment is characterized by a long interval of low-intensity storms (RIF <1), the retreat distance is shorter and the downslope sorting is less pronounced relative to the experiments with 2,000 or 1,000 fixed storm intervals.

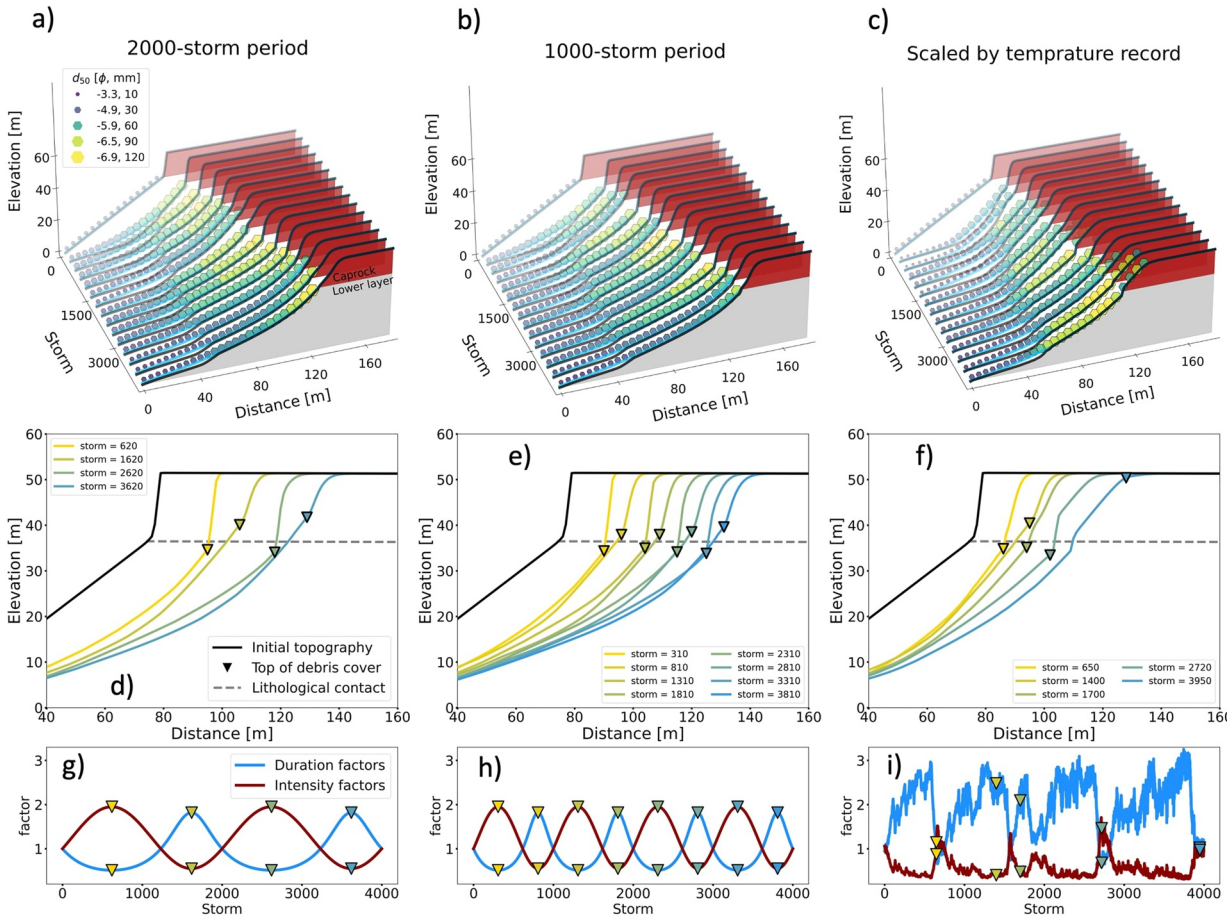

Figure 10. Changes in hillslope topography and grain size during the variable storm experiment set (2,000-storm period, 1,000-storm period, and scaled by temperature experiments, panels (a–c) respectively). Panels (d–f) show the topographic profiles and storm-varying debris-cover extent (opposite triangles), and panels (g–i) show the history of changes in rainstorm intensity factor (red line), and rainstorm duration factor (blue line), for the experiment in (a–c) respectively. Pairs of triangles (with the same location along the *x*-axis) in panels (g–i) denote the storms and the corresponding intensity (RIF) and duration (rainfall duration factor, RDF) factors at the time in which the profiles in panels (d–f) are shown. The storms resulting from all the combinations of RIF and RDF are shown by gray solid lines in Figure 3b.

6. Discussion

6.1. Intra-Storm Hillslope Hydrogeomorphic Dynamics

Our simulations confirm the intra-storm discontinuity of runoff flow and sediment transport, both in time and space, as observed and measured on arid slopes (Yair & Klein, 1973; Yair & Raz-Yassif, 2004). A hydrologic steady state is often not reached as the rainfall duration is often shorter than the runoff concentration time and accordingly, the peak sediment flux occurs immediately or shortly after the peak rainfall rate (>15 min), with increasing lag time from the beginning of the storm with increasing distance downslope (Figure S3 in Supporting Information S1). Consequently, sediment is mobilized at different locations along the slope at different times. For example, the peak sediment flux on the lower parts of the slopes commonly occurs more than 5 min after the peak flux in the upper parts (Figure S3 in Supporting Information S1). In many cases, only a fraction of the sediment is mobilized by the overland flow. As suggested by early studies (e.g., Gerson & Grossman, 1987; Howard & Selby, 2009) when the cliff breaks into large pieces (d_{50} > 100 mm), sediment transport is limited by the rate at which large material breaks into smaller pieces.

Surface wash redistributes the grains along the slope and the spatial distribution of particle size depends strongly on the rainfall intensity and the size of sediment supplied from the cliff. When the cliff breaks into small pieces (CGS = 10 mm), all size fractions are mobilized and the grain size along the slope is relatively homogeneous (Figure 6). However, cliff-derived debris size at the scale of 10 mm is likely limited to very fragile lithologies,

and commonly, much larger material is observed below cliffs (e.g., Verdian et al., 2021). When CGS is >10 mm, grains up to 100 mm are transported from the upper parts of the slope, leaving behind all coarser fractions (Figures 6 and 7). As a result, the median grain size increases at the upper parts and can reach a size greater than the median grain size of the cliff-derived debris (Figure 7b). Washing of finer grains from the upper parts and their deposition in the mid-to-lower parts of the slope (Figure 7) confirm previously suggested mechanisms for a preferential downslope reduction in grain size (Carson & Kirkby, 1972; Dury, 1966), and is consistent with other observations that document grain-size coarsening with runoff rate (Michaelides et al., 2012). Although there are other possible explanations for downslope sorting on arid slopes (McGrath et al., 2013), our experiments indicate that overland flow could play a major role in facilitating this process. Under the boundary condition in our experiments (no base level fall and all sediments/runoff are carried away at the outlet), runoff-driven size-dependent sediment transport promotes concave-upwards hillslope profiles as the grainsizes in the upper parts are coarsening. Our experiments indicate that for a given storm intensity the concavity increased with larger CGS and vice versa (Figure 7). Although it has been shown that in places where the erosion-effective storms are shorter than the runoff concentration time and hydraulic steady-states are rarely reached (as in our experiments) a convex-upward hillslope profile might develop, we suggest it is limited to hillslopes with homogeneous grainsize.

6.2. Hillslope Resistance to Rainstorm Forcing

To discuss the influence of rainstorm forcing on hillslope topography, as arises from our experiments, it is worthwhile to compare the magnitude of the storms we simulate to rainfall statistics from drylands worldwide. The base-storm we defined here represents a 100-year storm in the central Negev. This storm is a 30-min-long storm with a maximum 10-min intensity of 88 mm h^{-1} and a total rainfall depth of 25 mm. The simulations presented in Figure 5 are the result of storms with the same temporal pattern and duration but with the 10-min intensity bins scaled by factors ranging between 0.5 and 1.5. According to the results presented in Figure 5, when RIF <1, the cliff becomes buried when the median cliff-derived grain size is >10 mm, while only when RIF ≥1 sediment is effectively removed from the slope and vertical cliff persist. Storms with RIF ≥1 correspond to return level ≥5 years in Alice Springs, Northern Territory, Australia (Bureau of Meteorology), ≥50 years in the Colorado Plateau (based on Green River, Price, and Hanksville stations, Utah, USA, source: NOAA) >50 years in the Death Valley (based on Death Valley station, NV, USA, source: NOAA) and ≥100 years in the Negev (Marra & Morin, 2015; Marra et al., 2017; Shmilovitz et al., 2020) both for the maximal 10-min interval and the total rainfall over 30 min. This indicates that in the simulated geomorphic setting, the exhumation of the cliff (from being buried) requires the action of infrequent storms (≫5 years return level) and emphasizes the importance of the large events in the evolution of dryland hillslopes (Enzel et al., 2012; Gerson & Grossman, 1987; Wolman & Miller, 1960). Furthermore, these results support our approach of simulating individual rainstorms rather than the common application of long-term average conditions (such as long-term mean daily or monthly rainfall/discharge) in landscape evolution studies (Yetemen et al., 2019; Yuan et al., 2022).

Cliff-derived grain size impacts the sensitivity of hillslopes to rainstorms. In the numerical experiments we conducted, when CGS is >100 mm, even under intense rainstorms (RIF = 1.5), the cliff becomes buried after 500–1,000 storms. In this case, in-situ fragmentation of the debris limits sediment transport. Conversely, when CGS <100 mm, the hillslope morphology and the persistence of vertical cliffs become highly dependent on the rainstorm magnitude. Thus, the caprock weathering pattern controls the resistance of the hillslope to rainstorm forcing. The sensitivity to rainstorms under CGS <100 mm results from threshold effects, in which clast transport is limited by the number of times the overland flow exerts a shear stress greater than the threshold value for movement. Our experiments on temporal patterns of different storms suggest that this is an important factor that determines how often transport thresholds are exceeded. Obviously, there are many other factors in addition to the size of cliff-derived debris that determine the sensitivity of the hillslope to rainstorm forcing and to other climatic properties (Schmidt, 2009). Among these factors are internal lithological and structural attributes of the caprock and of the lower layer, the thickness ratio between these units, and the physical characteristics of soil and debris cover, including hydraulic conductivity and roughness. Vegetation cover and soil properties are themselves climate-dependent and have been shown to have a significant influence on erosion processes (Istanbulluoglu, 2009; Istanbulluoglu & Bras, 2006; Marston, 2010). However, here the focus is on the drier edge of Earth's drylands, where vegetation is either scarce or absent. Therefore, we did not consider changes in vegetation cover, with the goal to test whether rainstorm patterns alone can account for observed differences in hillslope morphology (Amit et al., 2006; Enzel et al., 2012).

6.3. Implication for Hillslope Evolution Under Climatic Change

In previous studies of the impact of climate on dryland hillslopes, triggers for hillslope geomorphic transitions were mostly discussed in terms of annual precipitation (Gerson & Grossman, 1987; Langbein & Schumm, 1958; Schmidt, 2009) while some considered or hypothesized that general trends in climate were also associated with changes in rainstorm patterns (Boroda et al., 2011; Schmidt, 2009). For example, Ahnert (1960) suggested that bare or partially covered rocky slopes below vertical cliffs, which are close to the angle of repose and are not the result of a lithologic transition, are indicative of previous debris cover that accumulated under wetter climates with gentler precipitation. Similarly, the simple climato-cyclic model (Gerson, 1982; Gerson & Grossman, 1987; Schmidt, 1989, 2009; Schmidt & Meitz, 1996) for the development of a sequence of talus flatirons suggests that drier climatic phases, characterized by increasing storminess, are responsible for slope dissection and subsequent detachment of the slope from the supplying cliff (Gerson, 1982; Gerson & Grossman, 1987; Schmidt et al., 2000).

Here, experiments with changes in storm regime, without changes in total rainfall, reproduce some of the above-mentioned features. For example, an alternating rainstorm intensity regime can significantly impact the extent of debris cover and could lead to the formation of complex caprock profiles with noticeable breaks in slope (Figure 10). Such features are occasionally observed in cliff-talus slopes that have evolved over long durations. The results also support the hypothesis that short and intense storms can enhance lateral cliff retreat (Figure 9). Our results suggest that the cumulative effect of dozens to hundreds of high-intensity storms can evacuate debris cover and undermine cliffs. As such, these results agree with the suggestion of Gerson (1982) that dry-phase dissection (assuming it is associated with more intense rainstorms) is relatively short-lived. It seems that relative to the time required for debris evacuation (Boroda et al., 2011; Roqué et al., 2013), a longer time interval is required to develop smooth debris cover. Thus, generally, our results are in line with some previous hypotheses regarding climate change's impact on hillslope evolution in drylands. However, while changes in annual rainfall were previously the focus, here we point to storm properties as a key aspect of climatic change and demonstrate the feasibility of having geomorphic transitions under permanent arid conditions solely by changes in rainstorm patterns (Boroda et al., 2011; Enzel et al., 2012). The quick response to changes in rainstorm properties implies that the duration of the storm phases determines whether the hillslope will maintain and display a climatic signal. For example, a quick alternation between storms of different intensities erases temporal differences in grain-size pattern and extent of debris cover (Figure 10b).

It is interesting to note that in most of our simulations, after a certain distance of lateral cliff retreat, debris eventually covers the cliff. This happens because the lower slope is lengthening, and as a result the average gradient decreases continuously. During rainstorm regimes in which high-intensity storms dominate, the cliff undergoes sustained retreat, but it is expected that after some additional retreat distance, debris will cover the cliff. Consequently, if the base level is fixed (as in all of our simulations), the transport capacity at the base of the cliff is insufficient to maintain steady retreat. A potential mechanism for achieving a quasi-steady-state without base level lowering is by a lateral translation of the boundary condition at the bottom of the slope in the same direction as the cliff retreat. For example, by a lateral migration of a local channel (Glade & Anderson, 2018). Development of concentrated flow features, such as rills and gullies, as the slope lengthens, may also contribute to long-term retreat.

6.4. Limitations and Future Work

Our modeling efforts and comparative field data demonstrate how changes in temporal patterns of rainstorms can contribute to significant geomorphic transitions along hillslopes. This study provides a mechanistic explanation for observations from hyperarid regions, where vegetation cover is low and the mean climate does not vary greatly over time. However, the proposed approach has limitations and assumptions that should be addressed in future research. First, in each simulation, we forced a constant lateral cliff retreat rate that reflects the cumulative effect of all the weathering processes acting on the cliff. This assumption is undoubtedly inaccurate as the weathering processes and weathering rates are expected to vary over time and between sites, depending on climatic factors such as temperature and humidity, lithology, and structure. In addition, caprock erosion processes not considered here, such as groundwater sapping, could be important in certain locations, and quantifying their impact on debris grain size will be beneficial. We also neglected climate-driven variations in vegetation cover, although in semi-arid environments, today and in the past, vegetation could have an important influence on caprock weathering and on the hillslope hydrological and erosional processes (Istanbulluoglu & Bras, 2006). Under future work, changes

in the hydrological properties of the debris layer through time (e.g., hydraulic conductivity), with and without relation to climate variations, should also be addressed as well to decipher specific climatic roles of hillslope erosion. In terms of rainfall forcing, there are still many open questions and improvements that are required. First, here we focus on the temporal pattern of storm intensity but future efforts should consider changes in the frequency-magnitude relations of storms that impact erosion and sediment flux, and contribute to topographic changes, especially in dry regions (Enzel et al., 2012; Leopold, 1951; Molnar, 2001; Tucker, 2004; Tucker & Bras, 2000). Moreover, all of the rainstorms simulated here have the same general pattern (intensity initially rises and then falls). Other general patterns and temporal properties should be examined. Lastly, we present here a 1-D model, and thus, there are unanswered questions regarding how spatial and temporal rainstorm properties affect the development of channel networks below cliffs. Based on the modeling tools and approaches presented here, fundamental questions in this direction could be answered. For example, model simulations could help identify necessary and sufficient conditions required to form hillslope remnants (talus flatirons), and reveal their relationship to the specific formative climatic forcing.

7. Conclusions

In this study, we presented a new 1-D LEM for hillslopes with caprock lithology in drylands, including explicit representations of storm-scale hydrology and erosion. Using the model, we evaluated hillslope response to rainstorm intensity and cliff weathering patterns under a fixed base-level. We focus on the impact of changes in storms' temporal structure based on modern observations that relate changes in maximal rainstorm intensity and increasing temperatures. Rainfall intensity and cliff weathering patterns, reflected by the grain size of the debris, determine whether or not the hillslope will be buried by its own debris. Numerical experiments based on inputs from a field site in the Negev desert (Israel) match the observed cross-sectional morphology of hillslopes, the thickness of cliff debris, and grain size patterns. Exploration of temporal patterns of rainstorms indicates that high-intensity storms result in an increased distance of cliff retreat and persistence of vertical cliffs relative to low-intensity rainstorms with the same total rainfall. These patterns emerge without changing the total storm rain depth. The alternation between rainstorm regimes of high and low intensity (keeping the total rainfall constant) resulted in varying extents of debris cover that controlled the caprock profile in a way similar to observations previously attributed to Quaternary-scale oscillations in mean climate. We emphasize that the results of the numerical experiments conducted here do not account for other factors that may vary with general trends in climate, such as vegetation cover. The results emphasize that hillslope evolution in the Earth's driest regions may be explained by changes in rainstorm intensity, its resulting hydrology, and the cliff weathering pattern.

Data Availability Statement

The model used here is based on the open-source Landlab software package (Barnhart et al., 2020; Hobley et al., 2017) with additional new functions for particle-size-dependent runoff-driven transport, debris-particle fragmentation, cliff weathering, and cliff-debris dry-ravel. The source code for the Landlab project is housed on GitHub: http://github.com/landlab/. Documentation, installation, instructions, and software dependencies for the entire Landlab project can be found at: http://landlab.github.io/. Source code for the additional functions and an accompanying Jupyter Notebook with a simulation example are currently available through the Zenodo repository http://doi.org/10.5281/zenodo.10612109.

Acknowledgments
This study was partially funded by the U.S.-Israel Binational Science Foundation (2020664 to YE and EM), the U.S. National Science Foundation (2100753, 2100702, 2104102, 2148762), and the BARD project (grant number: IS-5124-18 to EM). YS was supported by fellowships from the Hebrew University Advanced School for Environmental Studies and the Keren Kayemeth LeIsrael-Jewish National Fund. MA was supported by an ETH Zürich postdoctoral fellowship (project no. 21-1 FEL67) and by the Stiftung für naturwissenschaftliche und technische Forschung as well as the ETH Zürich Foundation.

References

Adams, J. M., Gasparini, N. M., Hobley, D. E., Tucker, G. E., Hutton, E. W., Nudurupati, S. S., & Istanbulluoglu, E. (2017). The landlab v1. 0 overlandflow component: A python tool for computing shallow-water flow across watersheds. *Geoscientific Model Development*, *10*(4), 1645–1663. https://doi.org/10.5194/gmd-10-1645-2017

AghaKouchak, A., Chiang, F., Huning, L. S., Love, C. A., Mallakpour, I., Mazdiyasni, O., et al. (2020). Climate extremes and compound hazards in a warming world. *Annual Review of Earth and Planetary Sciences*, *48*(1), 519–548. https://doi.org/10.1146/annurev-earth-071719-055228

Ahnert, F. (1960). The influence of pleistocene climates upon the morphology of cuesta scarps on the Colorado Plateau 1. *Annals of the Association of American Geographers*, *50*(2), 139–156. https://doi.org/10.1111/j.1467-8306.1960.tb00341.x

Ahnert, F. (1976). Brief description of a comprehensive three-dimensional process-response model for landform development. *Zeitschrift fur Geomorphologie, NF, Supplementband*, *25*, 29–49.

Amit, R., Enzel, Y., & Sharon, D. (2006). Permanent quaternary hyperaridity in the negev, Israel, resulting from regional tectonics blocking mediterranean frontal systems. *Geology*, *34*(6), 509–512. https://doi.org/10.1130/g22354.1

Anderson, R. S., Rajaram, H., & Anderson, S. P. (2019). Climate driven coevolution of weathering profiles and hillslope topography generates dramatic differences in critical zone architecture. *Hydrological Processes*, *33*(1), 4–19. https://doi.org/10.1002/hyp.13307

Andrews, E. D. (1983). Entrainment of gravel from naturally sorted riverbed material. *Geological Society of America Bulletin*, *94*(10), 1225–1231. https://doi.org/10.1130/0016-7606(1983)94<1225:eogfns>2.0.co;2
Armstrong, A. (1976). A three dimensional simulation of slope forms. *Zeitschrift für Geomorphologie*, *25*, 20–28.
Ashworth, P. J., & Ferguson, R. I. (1989). Size-selective entrainment of bed load in gravel bed streams. *Water Resources Research*, *25*(4), 627–634. https://doi.org/10.1029/wr025i004p00627
Attema, J. J., Loriaux, J. M., & Lenderink, G. (2014). Extreme precipitation response to climate perturbations in an atmospheric mesoscale model. *Environmental Research Letters*, *9*(1), 014003. https://doi.org/10.1088/1748-9326/9/1/014003
Bakker, J. P., & Le Heux, J. (1947). *Theory on central rectilinear recession of slopes*. North-Holland Publication.
Barnhart, K. R., Hutton, E. W., Tucker, G. E., Gasparini, N. M., Istanbulluoglu, E., Hobley, D. E., et al. (2020). Landlab v2. 0: A software package for earth surface dynamics. *Earth Surface Dynamics*, *8*(2), 379–397. https://doi.org/10.5194/esurf-8-379-2020
Bell, M. A., & Fox, N. A. (1996). Crawling experience is related to changes in cortical organization during infancy: Evidence from EEG coherence. *Developmental Psychobiology*, *29*(7), 551–561. https://doi.org/10.1002/(sici)1098-2302(199611)29:7<551::aid-dev1>3.0.co;2-t
Ben Dor, Y., Neugebauer, I., Enzel, Y., Schwab, M. J., Tjallingii, R., Erel, Y., & Brauer, A. (2019). Varves of the dead sea sedimentary record. *Quaternary Science Reviews*, *215*, 173–184. https://doi.org/10.1016/j.quascirev.2019.04.011
Boroda, R., Amit, R., Matmon, A., Finkel, R., Porat, N., Enzel, Y., et al. (2011). Quaternary-scale evolution of sequences of talus flatirons in the hyperarid negev. *Geomorphology*, *127*(1–2), 41–52. https://doi.org/10.1016/j.geomorph.2010.12.003
Boroda, R., Matmon, A., Amit, R., Haviv, I., Porat, N., Rood, D., et al. (2013). Long-term talus flatirons formation in the hyperarid northeastern negev, Israel. *Quaternary Research*, *79*(2), 256–267. https://doi.org/10.1016/j.yqres.2012.11.012
Bracken, L., & Kirkby, M. (2005). Differences in hillslope runoff and sediment transport rates within two semi-arid catchments in southeast Spain. *Geomorphology*, *68*(3–4), 183–200. https://doi.org/10.1016/j.geomorph.2004.11.013
Brunsden, D., & Prior, D. B. (1984). Slope instability.
Bryan, K. (1940). Gully gravure-a method of slope retreat. *Journal of Geomorphology*, *3*, 89–107.
Bull, W. B. (1991). Geomorphic responses to climatic change.
Bull, W. B., & Schick, A. P. (1979). Impact of climatic change on an arid watershed: Nahal Yael, southern Israel. *Quaternary Research*, *11*(2), 153–171. https://doi.org/10.1016/0033-5894(79)90001-2
Campforts, B., Shobe, C. M., Steer, P., Vanmaercke, M., Lague, D., & Braun, J. (2020). Hylands 1.0: A hybrid landscape evolution model to simulate the impact of landslides and landslide-derived sediment on landscape evolution. *Geoscientific Model Development*, *13*(9), 3863–3886. https://doi.org/10.5194/gmd-13-3863-2020
Carretier, S., Martinod, P., Reich, M., & Godderis, Y. (2016). Modelling sediment clasts transport during landscape evolution. *Earth Surface Dynamics*, *4*(1), 237–251. https://doi.org/10.5194/esurf-4-237-2016
Carson, M. A., & Kirkby, M. J. (1972). Hillslope form and process.
Chen, A., Darbon, J., & Morel, J.-M. (2014). Landscape evolution models: A review of their fundamental equations. *Geomorphology*, *219*, 68–86. https://doi.org/10.1016/j.geomorph.2014.04.037
Cohen, S., Willgoose, G., & Hancock, G. (2009). The mARM spatially distributed soil evolution model: A computationally efficient modeling framework and analysis of hillslope soil surface organization. *Journal of Geophysical Research*, *114*, F3. https://doi.org/10.1029/2008jf001214
Cohen, S., Willgoose, G., & Hancock, G. (2010). The mARM3D spatially distributed soil evolution model: Three-dimensional model framework and analysis of hillslope and landform responses. *Journal of Geophysical Research*, *115*(F4), F04013. https://doi.org/10.1029/2009jf001536
Cohen, S., Willgoose, G., Svoray, T., Hancock, G., & Sela, S. (2015). The effects of sediment transport, weathering, and aeolian mechanisms on soil evolution. *Journal of Geophysical Research: Earth Surface*, *120*(2), 260–274. https://doi.org/10.1002/2014jf003186
Coulthard, T. J., Neal, J. C., Bates, P. D., Ramirez, J., de Almeida, G. A., & Hancock, G. R. (2013). Integrating the LISFLOOD-FP 2D hydrodynamic model with the CAESAR model: Implications for modelling landscape evolution. *Earth Surface Processes and Landforms*, *38*(15), 1897–1906. https://doi.org/10.1002/esp.3478
D'Arcy, M., Whittaker, A. C., & Roda-Boluda, D. C. (2017). Measuring alluvial fan sensitivity to past climate changes using a self-similarity approach to grain-size fining, death valley, California. *Sedimentology*, *64*(2), 388–424. https://doi.org/10.1111/sed.12308
de Almeida, G. A., Bates, P., Freer, J. E., & Souvignet, M. (2012). Improving the stability of a simple formulation of the shallow water equations for 2-D flood modeling. *Water Resources Research*, *48*(5), 5528. https://doi.org/10.1029/2011wr011570
de Figueiredo, T., & Poesen, J. (1998). Effects of surface rock fragment characteristics on interrill runoff and erosion of a silty loam soil. *Soil and Tillage Research*, *46*(1–2), 81–95. https://doi.org/10.1016/s0167-1987(98)80110-4
Duller, R., Whittaker, A., Fedele, J., Whitchurch, A., Springett, J., Smithells, R., et al. (2010). From grain size to tectonics. *Journal of Geophysical Research*, *115*(F3), F03022. https://doi.org/10.1029/2009jf001495
Dunkerley, D. (2021). The importance of incorporating rain intensity profiles in rainfall simulation studies of infiltration, runoff production, soil erosion, and related landsurface processes. *Journal of Hydrology*, *603*, 126834. https://doi.org/10.1016/j.jhydrol.2021.126834
Dury, G. (1966). Pediment slope and particle size at middle pinnacle, near broken hill, new south wales. *Australian Geographical Studies*, *4*(1), 1–17. https://doi.org/10.1111/j.1467-8470.1966.tb00046.x
Duszyński, F., Migoń, P., & Strzelecki, M. C. (2019). Escarpment retreat in sedimentary tablelands and cuesta landscapes–landforms, mechanisms and patterns. *Earth-Science Reviews*, *196*, 102890. https://doi.org/10.1016/j.earscirev.2019.102890
Dutton, C. E. (1882). Tertiary history of the grand canyon district. *American Journal of Science*, *3*(140), 81–89. https://doi.org/10.2475/ajs.s3-24.140.81
Enzel, Y., Amit, R., Grodek, T., Ayalon, A., Lekach, J., Porat, N., et al. (2012). Late quaternary weathering, erosion, and deposition in Nahal Yael, Israel: An "impact of climatic change on an arid watershed"? *Bulletin*, *124*(5–6), 705–722. https://doi.org/10.1130/b30538.1
Fisher, O. (1866). Iv.—On the disintegration of a chalk cliff. *Geological Magazine*, *3*(26), 354–356. https://doi.org/10.1017/s0016756800167573
Fowler, H. J., Wasko, C., & Prein, A. F. (2021). Intensification of short-duration rainfall extremes and implications for flood risk: Current state of the art and future directions. *Philosophical Transactions of the Royal Society A*, *379*(2195), 20190541. https://doi.org/10.1098/rsta.2019.0541
French, H. M. (2017). *The periglacial environment*. John Wiley & Sons.
Gaillardet, J., Calmels, D., Romero-Mujalli, G., Zakharova, E., & Hartmann, J. (2019). Global climate control on carbonate weathering intensity. *Chemical Geology*, *527*, 118762. https://doi.org/10.1016/j.chemgeo.2018.05.009
Gerson, R. (1982). Talus relicts in deserts: A key to major climatic fluctuations.
Gerson, R., & Grossman, S. (1987). Geomorphic activity on escarpments and associated fluvial systems in hot deserts. In *Climate, history, periodicity, predictability* (Vol. 300-22).
Glade, R. C., & Anderson, R. (2018). Quasi-steady evolution of hillslopes in layered landscapes: An analytic approach. *Journal of Geophysical Research: Earth Surface*, *123*(1), 26–45. https://doi.org/10.1002/2017jf004466

Glade, R. C., Anderson, R. S., & Tucker, G. E. (2017). Block-controlled hillslope form and persistence of topography in rocky landscapes. *Geology*, *45*(4), 311–314. https://doi.org/10.1130/g38665.1

Goodrich, D. C., Faurès, J.-M., Woolhiser, D. A., Lane, L. J., & Sorooshian, S. (1995). Measurement and analysis of small-scale convective storm rainfall variability. *Journal of Hydrology*, *173*(1–4), 283–308. https://doi.org/10.1016/0022-1694(95)02703-r

Goudie, A. (1993). Salt weathering simulation using a single-immersion technique. *Earth Surface Processes and Landforms*, *18*(4), 369–376. https://doi.org/10.1002/esp.3290180406

Green, W. H., & Ampt, G. (1911). Studies on soil physics. *The Journal of Agricultural Science*, *4*(1), 1–24. https://doi.org/10.1017/s0021859600001441

Greenbaum, N., Mushkin, A., Porat, N., & Amit, R. (2020). Runoff generation, rill erosion and time-scales for hyper-arid abandoned alluvial surfaces, the Negev desert, Israel. *Geomorphology*, *358*, 107101. https://doi.org/10.1016/j.geomorph.2020.107101

Grossman, S., & Gerson, R. (1987). Fluviatile deposits and morphology of alluvial surfaces as indicators of quaternary environmental changes in the southern Negev, Israel. *Geological Society, London, Special Publications*, *35*(1), 17–29. https://doi.org/10.1144/gsl.sp.1987.035.01.03

Gutiérrez, M., Gutiérrez, F., & Desir, G. (2006). Considerations on the chronological and causal relationships between talus flatirons and palaeoclimatic changes in central and northeastern Spain. *Geomorphology*, *73*(1–2), 50–63. https://doi.org/10.1016/j.geomorph.2005.06.006

Gutiérrez, M., Lucha, P., Gutiérrez, F., Moreno, A., Guerrero, J., Martín-Serrano, A., et al. (2010). Are talus flatiron sequences in Spain climate-controlled landforms. *Zeitschrift für Geomorphologie*, *54*(2), 243–252. https://doi.org/10.1127/0372-8854/2010/0054-0013

Heimsath, A. M., Dietrich, W. E., Nishiizumi, K., & Finkel, R. C. (1997). The soil production function and landscape equilibrium. *Nature*, *388*(6640), 358–361. https://doi.org/10.1038/41056

Hobley, D. E., Adams, J. M., Nudurupati, S. S., Hutton, E. W., Gasparini, N. M., Istanbulluoglu, E., & Tucker, G. E. (2017). Creative computing with landlab: An open-source toolkit for building, coupling, and exploring two-dimensional numerical models of earth-surface dynamics. *Earth Surface Dynamics*, *5*(1), 21–46. https://doi.org/10.5194/esurf-5-21-2017

Howard, A. D., & Kerby, G. (1983). Channel changes in badlands. *Geological Society of America Bulletin*, *94*(6), 739–752. https://doi.org/10.1130/0016-7606(1983)94<739:ccib>2.0.co;2

Howard, A. D., & Kochel, R. (1988). Introduction to cuesta landforms and sapping. In *Sapping features of the Colorado Plateau: A comparative planetary geology field guide* (Vol. 491, p. 6).

Howard, A. D., & Selby, M. (1994). *Geomorphology of desert environments* (pp. 213–242). Chapman-Hall.

Howard, A. D., & Selby, M. J. (2009). Rock slopes. In A. J. Parsons & A. D. Abrahams (Eds.), *Geomorphology of desert environments* (pp. 189–232). Springer Netherlands. https://doi.org/10.1007/978-1-4020-5719-9_8

Hutchinson, J. (1998). A small-scale field check on the Fisher–Lehmann and Bakker–Le Heux cliff degradation models. *Earth Surface Processes and Landforms: The Journal of the British Geomorphological Group*, *23*(10), 913–926. https://doi.org/10.1002/(sici)1096-9837(199810)23:10<913::aid-esp911>3.0.co;2-g

Hutchinson, J., & Stuart, J. (2003). Analyses of the morphological changes with time, through denudation and siltation, in ditches of trapezoidal and triangular section. *Journal of Archaeological Science*, *30*(7), 797–808. https://doi.org/10.1016/s0305-4403(02)00241-8

Istanbulluoglu, E. (2009). An eco-hydro-geomorphic perspective to modeling the role of climate in catchment evolution. *Geography Compass*, *3*(3), 1151–1175. https://doi.org/10.1111/j.1749-8198.2009.00229.x

Istanbulluoglu, E., & Bras, R. L. (2006). On the dynamics of soil moisture, vegetation, and erosion: Implications of climate variability and change. *Water Resources Research*, *42*(6), W06418. https://doi.org/10.1029/2005wr004113

Johnstone, S. A., & Hilley, G. E. (2015). Lithologic control on the form of soil-mantled hillslopes. *Geology*, *43*(1), 83–86. https://doi.org/10.1130/g36052.1

Jouzel, J., Masson-Delmotte, V., Cattani, O., Dreyfus, G., Falourd, S., Hoffmann, G., et al. (2007). Orbital and millennial Antarctic climate variability over the past 800,000 years. *Science*, *317*(5839), 793–796. https://doi.org/10.1126/science.1141038

Kendon, E. J., Fischer, E. M., & Short, C. J. (2023). Variability conceals emerging trend in 100 yr projections of UK local hourly rainfall extremes. *Nature Communications*, *14*(1), 1133. https://doi.org/10.1038/s41467-023-36499-9

King, L. C. (1953). Canons of landscape evolution. *Geological Society of America Bulletin*, *64*(7), 721–752. https://doi.org/10.1130/0016-7606(1953)64[721:cole]2.0.co;2

Kirkby, M. (1988). Hillslope runoff processes and models. *Journal of Hydrology*, *100*(1–3), 315–339. https://doi.org/10.1016/0022-1694(88)90190-4

Komar, P. D. (1987). Selective gravel entrainment and the empirical evaluation of flow competence. *Sedimentology*, *34*(6), 1165–1176. https://doi.org/10.1111/j.1365-3091.1987.tb00599.x

Koons, E. D. (1955). Cliff retreat in the southwestern United States. *American Journal of Science*, *253*(1), 44–52. https://doi.org/10.2475/ajs.253.1.44

Lamp, J., Marchant, D., Mackay, S., & Head, J. (2017). Thermal stress weathering and the spalling of Antarctic rocks. *Journal of Geophysical Research: Earth Surface*, *122*(1), 3–24. https://doi.org/10.1002/2016jf003992

Langbein, W. B., & Schumm, S. A. (1958). Yield of sediment in relation to mean annual precipitation. *Eos, Transactions American Geophysical Union*, *39*(6), 1076–1084.

Lehmann, O. (1933). Morphologische theorie der verwitterung von steinschlagwanden. *Vierteljahrsschrift der Naturforschenden Gesellschaft in Zürich*, *78*(21), 83–126.

Lenderink, G., de Vries, H., Fowler, H. J., Barbero, R., van Ulft, B., & van Meijgaard, E. (2021). Scaling and responses of extreme hourly precipitation in three climate experiments with a convection-permitting model. *Philosophical Transactions of the Royal Society A*, *379*(2195), 20190544. https://doi.org/10.1098/rsta.2019.0544

Lenderink, G., & Van Meijgaard, E. (2008). Increase in hourly precipitation extremes beyond expectations from temperature changes. *Nature Geoscience*, *1*(8), 511–514. https://doi.org/10.1038/ngeo262

Leopold, L. B. (1951). Rainfall frequency: An aspect of climatic variation. *Eos, Transactions American Geophysical Union*, *32*(3), 347–357.

Li, P., Chen, J., Zhao, G., Holden, J., Liu, B., Chan, F. K. S., et al. (2022). Determining the drivers and rates of soil erosion on the loess plateau since 1901. *Science of the Total Environment*, *823*, 153674. https://doi.org/10.1016/j.scitotenv.2022.153674

Marra, F., & Morin, E. (2015). Use of radar QPE for the derivation of intensity–duration–frequency curves in a range of climatic regimes. *Journal of Hydrology*, *531*, 427–440. https://doi.org/10.1016/j.jhydrol.2015.08.064

Marra, F., & Morin, E. (2018). Autocorrelation structure of convective rainfall in semiarid-arid climate derived from high-resolution x-band radar estimates. *Atmospheric Research*, *200*, 126–138. https://doi.org/10.1016/j.atmosres.2017.09.020

Marra, F., Morin, E., Peleg, N., Mei, Y., & Anagnostou, E. N. (2017). Intensity–duration–frequency curves from remote sensing rainfall estimates: Comparing satellite and weather radar over the eastern Mediterranean. *Hydrology and Earth System Sciences*, *21*(5), 2389–2404. https://doi.org/10.5194/hess-21-2389-2017

Marston, R. A. (2010). Geomorphology and vegetation on hillslopes: Interactions, dependencies, and feedback loops. *Geomorphology*, *116*(3–4), 206–217. https://doi.org/10.1016/j.geomorph.2009.09.028

McCarroll, N. R., Pederson, J. L., Hidy, A. J., & Rittenour, T. M. (2021). Chronostratigraphy of talus flatirons and piedmont alluvium along the book cliffs, Utah–testing models of dryland escarpment evolution. *Quaternary Science Reviews*, *274*, 107286. https://doi.org/10.1016/j.quascirev.2021.107286

McGrath, G. S., Nie, Z., Dyskin, A., Byrd, T., Jenner, R., Holbeche, G., & Hinz, C. (2013). In situ fragmentation and rock particle sorting on arid hills. *Journal of Geophysical Research: Earth Surface*, *118*(1), 17–28. https://doi.org/10.1029/2012jf002402

Meyer-Peter, E., & Müller, R. (1948). Formulas for bed-load transport. In *IAHSR 2nd meeting, Stockholm, Appendix 2*.

Michaelides, K., Lister, D., Wainwright, J., & Parsons, A. J. (2012). Linking runoff and erosion dynamics to nutrient fluxes in a degrading dryland landscape. *Journal of Geophysical Research*, *117*(G4), G00N15. https://doi.org/10.1029/2012jg002071

Molnar, P. (2001). Climate change, flooding in arid environments, and erosion rates. *Geology*, *29*(12), 1071–1074. https://doi.org/10.1130/0091-7613(2001)029<1071:ccfiae>2.0.co;2

Naylor, L. A., Spencer, T., Lane, S. N., Darby, S. E., Magilligan, F. J., Macklin, M. G., & Möller, I. (2017). Stormy geomorphology: Geomorphic contributions in an age of climate extremes. *Earth Surface Processes and Landforms*, *42*(1), 166–190. https://doi.org/10.1002/esp.4062

Neely, A. B., & DiBiase, R. A. (2020). Drainage area, bedrock fracture spacing, and weathering controls on landscape-scale patterns in surface sediment grain size. *Journal of Geophysical Research: Earth Surface*, *125*(10), e2020JF005560. https://doi.org/10.1029/2020jf005560

Nicholson, S. E. (2011). Dryland climatology.

Patricola, C. M., Wehner, M. F., Bercos-Hickey, E., Maciel, F. V., May, C., Mak, M., et al. (2022). Future changes in extreme precipitation over the San Francisco bay area: Dependence on atmospheric river and extratropical cyclone events. *Weather and Climate Extremes*, *36*, 100440. https://doi.org/10.1016/j.wace.2022.100440

Pena-Monné, J. L., Sampietro-Vattuone, M. M., & Picazo-Millán, J. V. (2022). Late Quaternary palaeoenvironmental controls on concentric talus evolution in the Central Ebro Basin (NE Spain). *Environmental Earth Sciences*, *81*(17), 422. https://doi.org/10.1007/s12665-022-10547-x

Penck, W. (1953). *Morphological analysis of landforms. translated by h. Czech and kc boswell*. Macmillan.

Poesen, J., & Lavee, H. (1994). Rock fragments in top soils: Significance and processes. *Catena*, *23*(1–2), 1–28. https://doi.org/10.1016/0341-8162(94)90050-7

Rengers, F. K., McGuire, L., Kean, J. W., Staley, D. M., & Hobley, D. (2016). Model simulations of flood and debris flow timing in steep catchments after wildfire. *Water Resources Research*, *52*(8), 6041–6061. https://doi.org/10.1002/2015wr018176

Román-Sánchez, A., Temme, A., Willgoose, G., van den Berg, D., Gura, C. M., & Vanwalleghem, T. (2021). The fingerprints of weathering: Grain size distribution changes along weathering sequences in different lithologies. *Geoderma*, *383*, 114753. https://doi.org/10.1016/j.geoderma.2020.114753

Roqué, C., Linares, R., Zarroca, M., Rosell, J., Pellicer, X. M., & Gutiérrez, F. (2013). Chronology and paleoenvironmental interpretation of talus flatiron sequences in a sub-humid mountainous area: Tremp depression, Spanish Pyrenees. *Earth Surface Processes and Landforms*, *38*(13), 1513–1522. https://doi.org/10.1002/esp.3391

Scheidegger, A. E. (2012). *Theoretical geomorphology*. Springer Science & Business Media.

Schmidt, K.-H. (1989). The significance of scarp retreat for cenozoic landform evolution on the Colorado plateau, USA. *Earth Surface Processes and Landforms*, *14*(2), 93–105. https://doi.org/10.1002/esp.3290140202

Schmidt, K. H. (2009). Hillslopes as evidence of climatic change. In *Geomorphology of desert environments* (pp. 675–694).

Schmidt, K. H., & Meitz, P. (1996). Cuesta scarp forms and processes in different altitudinal belts of the Colorado plateau as indicators of climate change'. In *Advances in hillslope processes* (pp. 1079–1097).

Schmidt, K. H., Meitz, P., & Cuesta, R. A. (2000). Effects of increasing humidity on slope geomorphology: Cuesta scarps on the Colorado Plateau, USA. In *The hydrology-geomorphology interface: Rainfall, floods, sedimentation, land use. A selection of papers presented at the conference on drainage basin dynamics and morphology held in Jerusalem, Israel, May 1999* (pp. 165–181).

Schumm, S. A., & Chorley, R. (1964). The fall of threatening rock. *American Journal of Science*, *262*(9), 1041–1054. https://doi.org/10.2475/ajs.262.9.1041

Schumm, S. A., & Chorley, R. (1966). *Talus weathering and scarp recession in the Colorado plateaus*. US Geological Survey.

Selby, M. J., Augustinus, P. C., Moon, V. G., & Stevenson, R. J. (1982). Hillslope materials and processes. Hillslope materials and processes.

Sharon, D. (1979). Correlation analysis of the Jordan Valley rainfall field. *Monthly Weather Review*, *107*(8), 1042–1047. https://doi.org/10.1175/1520-0493(1979)107<1042:caotjv>2.0.co;2

Sheehan, C. E., & Ward, D. J. (2018). Late Pleistocene talus flatiron formation below the coal cliffs cuesta, Utah, USA. *Earth Surface Processes and Landforms*, *43*(9), 1973–1992. https://doi.org/10.1002/esp.4369

Shmilovitz, Y., Enzel, Y., Morin, E., Armon, M., Matmon, A., Mushkin, A., et al. (2022). Aspect-dependent bedrock weathering, cliff retreat, and cliff morphology in a hyperarid environment. *GSA Bulletin*. https://doi.org/10.1130/b36442.1

Shmilovitz, Y., Marra, F., Enzel, Y., Morin, E., Armon, M., Matmon, A., et al. (2023). The impact of extreme rainstorms on escarpment morphology in arid areas: Insights from the central Negev Desert. *Journal of Geophysical Research: Earth Surface*, *128*(10), e2023JF007093. https://doi.org/10.1029/2023jf007093

Shmilovitz, Y., Morin, E., Rinat, Y., Haviv, I., Carmi, G., Mushkin, A., & Enzel, Y. (2020). Linking frequency of rainstorms, runoff generation and sediment transport across hyperarid talus-pediment slopes. *Earth Surface Processes and Landforms*, *45*(7), 1644–1659. https://doi.org/10.1002/esp.4836

Skinner, C. J., Peleg, N., Quinn, N., Coulthard, T. J., Molnar, P., & Freer, J. (2020). The impact of different rainfall products on landscape modelling simulations. *Earth Surface Processes and Landforms*, *45*(11), 2512–2523. https://doi.org/10.1002/esp.4894

Te Chow, V., Maidment, D. R., & Mays, L. W. (1988). Applied hydrology.

Temme, A., Armitage, J., Attal, M., van Gorp, W., Coulthard, T., & Schoorl, J. (2017). Developing, choosing and using landscape evolution models to inform field-based landscape reconstruction studies. *Earth Surface Processes and Landforms*, *42*(13), 2167–2183. https://doi.org/10.1002/esp.4162

Terzaghi, K. (1962). Stability of steep slopes on hard unweathered rock. *Géotechnique*, *12*(4), 251–270. https://doi.org/10.1680/geot.1962.12.4.251

Tucker, G. E. (2004). Drainage basin sensitivity to tectonic and climatic forcing: Implications of a stochastic model for the role of entrainment and erosion thresholds. *Earth Surface Processes and Landforms*, *29*(2), 185–205. https://doi.org/10.1002/esp.1020

Tucker, G. E., & Bras, R. L. (2000). A stochastic approach to modeling the role of rainfall variability in drainage basin evolution. *Water Resources Research*, *36*(7), 1953–1964. https://doi.org/10.1029/2000wr900065

Tucker, G. E., & Hancock, G. R. (2010). Modelling landscape evolution. *Earth Surface Processes and Landforms*, *35*(1), 28–50. https://doi.org/10.1002/esp.1952

Twidale, C. (1959). Some problems of slope development. *Journal of the Geological Society of Australia*, *6*(2), 131–147. https://doi.org/10.1080/00167615908728503

Twidale, C., & Milnes, A. (1983). Slope processes active late in arid scarp retreat. *Zeitschrift für Geomorphologie*, *27*(3), 343–361. https://doi.org/10.1127/zfg/27/1983/343

Valters, D. (2016). Modelling geomorphic systems: Landscape evolution. In *Geomorphological techniques*. British Society for Geomorphology.

Verdian, J. P., Sklar, L. S., Riebe, C. S., & Moore, J. R. (2021). Sediment size on talus slopes correlates with fracture spacing on bedrock cliffs: Implications for predicting initial sediment size distributions on hillslopes. *Earth Surface Dynamics*, *9*(4), 1073–1090. https://doi.org/10.5194/esurf-9-1073-2021

Ward, D., Berlin, M., & Anderson, R. (2011). Sediment dynamics below retreating cliffs. *Earth Surface Processes and Landforms*, *36*(8), 1023–1043. https://doi.org/10.1002/esp.2129

Wells, T., Willgoose, G., & Hancock, G. (2008). Modeling weathering pathways and processes of the fragmentation of salt weathered quartz-chlorite schist. *Journal of Geophysical Research*, *113*, F1. https://doi.org/10.1029/2006jf000714

Westra, S., Fowler, H. J., Evans, J. P., Alexander, L. V., Berg, P., Johnson, F., et al. (2014). Future changes to the intensity and frequency of short-duration extreme rainfall. *Reviews of Geophysics*, *52*(3), 522–555. https://doi.org/10.1002/2014rg000464

White, W., & Day, T. (1982). Transport of graded gravel bed material. In *Gravel-bed rivers* (pp. 181–223).

Whittaker, A. C., Attal, M., & Allen, P. A. (2010). Characterising the origin, nature and fate of sediment exported from catchments perturbed by active tectonics. *Basin Research*, *22*(6), 809–828. https://doi.org/10.1111/j.1365-2117.2009.00447.x

Wilcox, B. P., Newman, B. D., Brandes, D., Davenport, D. W., & Reid, K. (1997). Runoff from a semiarid ponderosa pine hillslope in New Mexico. *Water Resources Research*, *33*(10), 2301–2314. https://doi.org/10.1029/97wr01691

Willgoose, G. (2005). Mathematical modeling of whole landscape evolution. *Annual Review of Earth and Planetary Sciences*, *33*(1), 443–459. https://doi.org/10.1146/annurev.earth.33.092203.122610

Wolman, M. G., & Miller, J. P. (1960). Magnitude and frequency of forces in geomorphic processes. *The Journal of Geology*, *68*(1), 54–74. https://doi.org/10.1086/626637

Wood, A. (1942). The development of hillside slopes. *Proceedings of the Geologists' Association*, *53*(3–4), 128-IN3. https://doi.org/10.1016/s0016-7878(42)80019-x

Yair, A., & Klein, M. (1973). The influence of surface properties on flow and erosion processes on debris covered slopes in an arid area. *Catena*, *1*, 1–18. https://doi.org/10.1016/s0341-8162(73)80002-5

Yair, A., & Lavee, H. (1990). Spatial variability of overland flow in a small arid basin. *International Association of Scientific Hydrology Publications*, *189*, 2–17.

Yair, A., & Raz-Yassif, N. (2004). Hydrological processes in a small arid catchment: Scale effects of rainfall and slope length. *Geomorphology*, *61*(1–2), 155–169. https://doi.org/10.1016/j.geomorph.2003.12.003

Yetemen, O., Saco, P. M., & Istanbulluoglu, E. (2019). Ecohydrology controls the geomorphic response to climate change. *Geophysical Research Letters*, *46*(15), 8852–8861. https://doi.org/10.1029/2019gl083874

Yuan, X., Guerit, L., Braun, J., Rouby, D., & Shobe, C. (2022). Thickness of fluvial deposits records climate oscillations. *Journal of Geophysical Research: Solid Earth*, *127*(4), e2021JB023510. https://doi.org/10.1029/2021jb023510

References From the Supporting Information

Al-Farraj, A., & Harvey, A. M. (2000). Desert pavement characteristics on wadi terrace and alluvial fan surfaces: Wadi Al-Bih, UAE and Oman. *Geomorphology*, *35*(3–4), 279–297. https://doi.org/10.1016/s0169-555x(00)00049-0